PAPER

Foundations of plasmas as ion sources

To cite this article: Benjamin Jorns and Trevor Lafleur 2023 *Plasma Sources Sci. Technol.* **32** 014001

IOP Publishing Plasma Sources Science and Technology
Plasma Sources Sci. Technol. **32** (2023) 014001 (30pp) https://doi.org/10.1088/1361-6595/aca560

Foundations of plasmas as ion sources

Benjamin Jorns[1,*] **and Trevor Lafleur**[2]

[1] Department of Aerospace Engineering, University of Michigan, Ann Arbor, MI, United States of America
[2] ThrustMe, Verrières-le-Buisson, France

E-mail: bjorns@umich.edu

Received 4 August 2022, revised 3 November 2022
Accepted for publication 23 November 2022
Published 9 January 2023

Abstract

An overview of low temperature, partially magnetized ion sources is presented. This class of devices is broadly characterized by plasma densities below 10^{19} m^{-3}, electron temperatures below 100 eV, and magnetic field strength tailored such that electrons are magnetized whereas ions are not. The overarching approach is pedagogical, targeting an audience that does not necessarily have an expertise in low temperature devices. A tutorial is presented on the basic physics of operation of common ion sources including an overview of standard methods for plasma generation and acceleration. Typical diagnostics and common uses of these plasma sources are also reviewed. Special attention is given to applications in plasma propulsion and materials processing. This class of ion sources is then discussed in the context of the current state of the field, key technical and scientific challenges, and future prospects.

Keywords: low temperature plasma, ion sources, plasma propulsion, materials processing, diagnostics

(Some figures may appear in colour only in the online journal)

1. Introduction

Ion sources are broadly defined as devices designed to produce and energize ions. They accomplish this by converting a working gas into a plasma state and employing a combination of electric and magnetic fields to accelerate the plasma's ions into a targeted direction and speed. While there are many types of ion sources, the ones we consider in this work consist of partially ionized, non-equilibrium plasmas with relatively low densities and temperatures [1]. 'Non-equilibrium' indicates the constituent species in the ionized gas—neutrals, ions, and electrons—are not necessarily in thermal equilibrium. 'Low density' refers to the electron/ion density, which is typically $<10^{19}$ m^{-3}. The nomenclature 'low-temperature' stems from the electron species, which has temperatures less than 100 eV in the systems of interest. Notable examples of ion sources in this operational regime include plasma thrusters that expel ion streams to produce thrust and ion beam generators to selectively bombard and shape material.

We differentiate the ion sources described in this Foundations paper by the plasma generator, i.e. how the plasma state is produced, and the plasma accelerator, i.e. the process for accelerating the ions. Plasma generators fall into two broad categories: direct current (DC) and alternating current (AC). In the former, an electron discharge—usually facilitated by a closed loop circuit with anode and thermionically emitting cathode—is employed to pass high energy electrons through the working gas. This results in impact ionization. In AC systems, a rapidly varying electromagnetic field is employed to energize the electrons, again leading to impact ionization. Acceleration processes are categorized by the fundamental forces employed to energize and direct the flow of the ions. These include electrothermal, electromagnetic, and electrostatic acceleration schemes.

The objective of this article is to provide a high-level overview of low-temperature ion sources. It is intended to be an introduction to those with a familiarity with plasma physics but not a detailed knowledge of the operation of these devices. We thus favor qualitative scaling arguments in lieu of more detailed analysis to motivate key dependencies and trends. To this end, we present in the first section a tutorial on the basic

* Author to whom any correspondence should be addressed.

physics of operation of ion sources, describing the types of plasma generators and accelerators. In the second section, we provide an overview of common diagnostics that are employed to characterize the operation of these sources. In the third section, we highlight key examples of the applications of these sources. In the fourth and final section, we discuss the future outlook for investigations into ion sources by referencing the current state of the field and key challenges with research and technology infusion.

2. Plasma generation

2.1. Overview

Figure 1 illustrates graphically the process for positive ion production through electron impact in a DC ion source without magnetic field. Here we have represented the system as a simplified volume of length, L, bounded by walls with area, A_w, and an exit area, A_e, through which created ions are extracted. To begin the ion production process, neutral gas flows into the chamber. Seed electrons are then introduced to this flow field, and an external power source is applied to increase the energy of the electrons. If the gain in electron energy is sufficiently high to exceed the neutral gas ionization energy, ϵ_{iz}, when an electron impacts a neutral particle, it has a finite probability of creating an ion and electron pair. In practice, if the electrons in the source have sufficiently high energy, these ions can be ionized again to higher charge states, though we neglect this process for this simplified overview. Conversely, in some cases, the ambient electrons can attach to the neutrals and produce negative ion states. This process is also not discussed here. We note as well that although figure 1 shows DC electrostatic acceleration as the energization process, AC acceleration or coupling with electromagnetic waves is also possible (see section 2.3 below). We describe in the following section common figures of merit for plasma generators and provide additional details on both the AC and DC methods.

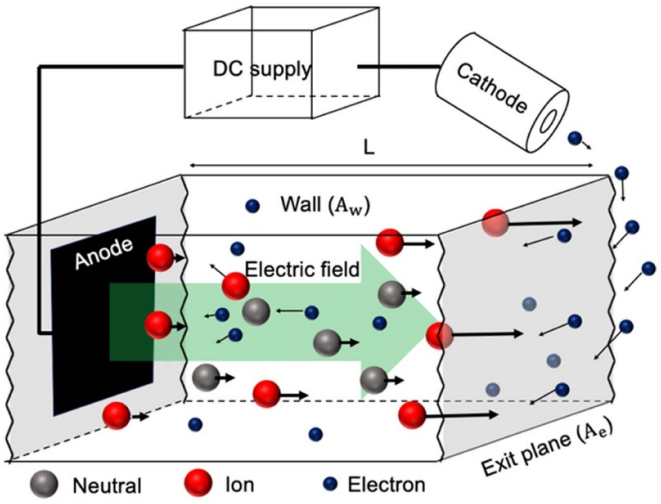

Figure 1. Control volume for a DC ion source with anode and cathode showing an ionization event. No magnetic field is applied in this illustration.

2.2. Figures of merit

2.2.1. Mass utilization. The mass utilization efficiency indicates the ability of the source to convert the working gas of neutrals into ions. For a device that primarily produces singly-charged ions, this is quantified as

$$\eta_m = \frac{I_i}{\dot{m}}\left(\frac{m_i}{q}\right), \tag{1}$$

where I_i is the current (charge carriers per unit time) extracted through the exit area of the system, $\dot{m}$ is the mass flow rate of gas into the system, q is the elementary unit charge, and m_i is the ion mass. Physically, this represents the ratio of the number of generated charges per unit time that are extracted to the number of atoms/molecules inserted per unit time into the generator. Higher values therefore represent a higher conversion rate of neutrals to ions. We note that this definition is modified by the fraction of charge states if and when there are multiply charged species (see [2]).

Generally, the mass utilization improves with the ratio, L/λ_{mfp}, where L is the characteristic length of the chamber and λ_{mfp} is the mean free path for ionization. This stems from the fact that since neutrals have a longer residence time in the device, they have a higher likelihood of experiencing impact ionization. This ratio can be improved by increasing the length of the generator, increasing the working gas density, or selecting a gas with a larger ionization cross section. The mass utilization also can be increased by reducing the degree of undesirable plasma flux to the walls. Implementing magnetic fields to confine the ionization-inducing electrons is a common technique to mitigate this flux. Such magnetic fields may be needed anyway in the operation of the ion source itself, particularly if plasma generation occurs with electromagnetic waves (section 2.3).

2.2.2. Ion production cost. The energy associated with the ion generation process is quantified with the ion production cost (see [2]):

$$\epsilon_b = \frac{P_s}{I_i}, \tag{2}$$

where P_s is the power supplied by the generator for ionization. This figure of merit is expressed in units of electron volts per ion. It physically represents the amount of energy that must be expended to produce one useable ion in the system. A smaller ion production cost therefore corresponds to a more efficient plasma generator.

Several factors influence the ion production cost. The first of these is inelastic losses. These include the energy to initially ionize the gas as well as the energy lost to excitation states. The latter processes contribute to the light emission exhibited by most ion sources. The ratio of the excitation losses to ionization losses is ultimately a function of the electron temperature [2, 3]. For many of the sources of interest, the temperature is sufficiently high that the ionization losses dominate. By

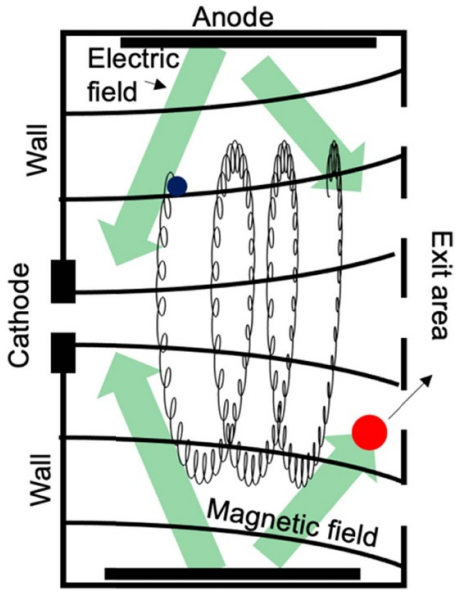

Figure 2. Example of cross-sectional schematic where magnetic field transverse to an applied electric field can improve electron confinement. Notional unmagnetized ion trajectory (red) and electron trajectory (blue) subject to an $E \times B$ drift are shown.

selecting working gases with lower ionization energies and fewer excitation states, it is possible to lower the ion production cost.

Imperfect electron confinement is a second driver for ion production cost. This effect depends on the volume to area ratio of the plasma source and scales with the ratio of the area of the walls to the area through which ions are extracted. Poor confinement ultimately can lead to production costs that are 1–2 orders of magnitude higher than the ionization energy, $\epsilon_b \gg \epsilon_{iz}$. The electron confinement can in principle be improved by adopting geometries with a larger volume to area ratio, though the available footprint of the system often can limit the practicality of this approach. As an alternative, a magnetic field can be employed such that magnetic contours are parallel to the generator walls. Magnetic field configurations vary based on the source, but the common criterion is that the strength of the magnetic field is such that electrons are magnetized but ions are not. Figure 2 shows one example of magnetic confinement employed in gridded ion sources. In this case, an electric field from anode to cathode crossed with the applied magnetic field results in an electron drift that inhibits motion directly to the anode and walls. This increases electron residence time and therefore improves ionization fraction. The heavier, unmagnetized ions, on the other hand, can be extracted by electrostatic force directly from the geometry through the exit area.

Related to the problem of electron confinement, the probability of ionization for the gas is a third factor that impacts the production cost. As with the mass utilization, this depends on the ratio, L/λ_{mfp}. The parameters influencing this metric are discussed in the previous section.

A fourth driver that can impact the ion production cost is the transfer efficiency from the generator to the plasma. This is particularly relevant to AC devices where power transfer schemes include radio-frequency (RF) voltages applied to electrodes, RF antennae that either couple inductively with the plasma or which launch propagating electromagnetic helicon waves [4], and microwave electron cyclotron resonance (ECR) [5]. Power absorption in these cases can strongly depend on the properties of the resident plasma and any applied magnetic field. For example, the resistive impedance of most low-pressure plasma discharges is typically much less than the characteristic output impedance of RF power generators (which is usually 50 Ω), resulting in significant power reflected to the generator and very poor power transfer to the plasma itself. This can be mitigated by employing special impedance matching networks, or in some cases, by tailoring the plasma density and magnetic field for improved coupling. However, even with a matching network and ideal impedance matching (i.e. zero reflected power), unavoidable losses still occur due to Ohmic heating of the antenna and/or electrical components in the matching network [6].

2.3. Types of plasma generators

2.3.1. DC generators. For a DC scheme, it is common to employ a thermionically emitting cathode (figure 1) to source electrons. These are then drawn by an electrostatic field established from the cathode to an anode. This field accelerates the electrons to sufficiently high energy to ionize molecules from the working gas. As discussed in the preceding section, in order to improve mass utilization and reduce ion production costs in a DC discharge, magnetic fields often are applied transverse to the anode and cathode electrodes (cf figure 2). The ignition criterion of in DC charges can be described by a Paschen law that depends on the applied electric field and working gas pressure [3]. Qualitatively, this law is based on the idea that the accelerating potential on the electrons must be sufficiently large so that they have enough energy to result in ionization on impact with the working gas. If the pressure of the working gas is too low, energized electrons will transit through the chamber without impacting a molecule. If the pressure is too high, electrons will not have sufficient space to accelerate to high enough energy before colliding with a molecule.

In practice, while the fundamentals of DC plasma generation remain the same for most devices, the implementation varies. For example, in gridded ion thrusters, plasma generation occurs in an upstream cylindrical discharge chamber in which a center-mounted cathode directs electron current to a concentric anode. A transverse magnetic field to this current is applied by an arrangement of magnets or electromagnets around the chamber. In Hall effect discharges, the electron current is established between an upstream annular anode and downstream cathode. Electron motion is then impeded by the presence of radial magnetic fields. In concepts like magnetoplasmadynamic (MPD) thrusters, a centrally mounted cathode establishes a current with a concentric anode. The current along the cathode axis drives an azimuthal magnetic field. Section 3 provides additional details on each of these implementations. We also note that in many of these applications,

the same electric and magnetic field setup is employed to both generate and accelerate ions from the working gas. The need to balance the acceleration process against ionization can lead to reductions in the performance metrics of the generator. We discuss the implications of this trade in section 3.

2.3.2. AC generators. AC plasma generators employ a combination of time-varying electric and magnetic fields to energize the electrons. This energization can be performed capacitively, inductively, or through the absorption of electromagnetic waves. For example, a common architecture found in materials processing, known as a capacitively coupled plasma (CCP), is to employ two parallel plates with an RF voltage applied across the electrodes. Power is then transferred to electrons by the time-varying electric fields, which then sustain the discharge through impact ionization of the background working gas. Plasma ignition criterion in these devices also follows a type of Paschen law and depends on the magnitude of the applied voltage, the operating pressure, electrode gap length, and RF frequency [3]. CCPs are discussed in more detail in sections 3.2 and 5.3.

Another common AC plasma generator is known as an inductively coupled plasma (ICP). Here an RF coil or antenna is either wrapped around a cylindrical dielectric tube or is in the shape of a flat spiral (much like a stove-top heating element) placed at one end and separated from the plasma by an insulator. By then applying an RF current to the coil, time-varying inductive electric fields are produced which can couple to plasma electrons and transfer power. Plasma ignition usually initially occurs when the coils operate in a capacitive (E) mode. This results in large voltage across the coil (which causes breakdown of the input gas). As the power increases, a sharp rise in plasma density is commonly observed as the system jumps into the inductive (H) mode (i.e. where power transfer now predominately occurs due to inductive coupling). ICPs are discussed in more detail in section 5.3.

Wave-based concepts are also commonly employed for AC plasma generation. For example, if a static magnetic field is applied, and depending on the source and antenna geometry, electromagnetic Helicon waves can be launched from an inductive antenna into the plasma [3, 7]. The dominant electromagnetic mode excited is largely determined by the geometry of the antenna itself, and wave propagation allows for the possibility of remote power deposition away from the source region. ECR is another commonly used wave-based plasma generation scheme. Here, electromagnetic waves in the GHz range are injected into an ion source through an external waveguide [3], or launched from a coaxial electrode configuration [8–10]. By then applying a properly designed static magnetic field, electrons can be made to rotate in resonance with the right-hand polarized component of the electromagnetic field [3, 5]. This results in efficient electron heating and subsequent ionization of the working gas. Plasma ignition in both Helicon and ECR sources is also governed by a Paschen like law that depends on the magnitude of the electric field of the mode and the working gas density.

3. Plasma acceleration

3.1. Overview

In the partially-magnetized ion sources considered in this work, magnetic and ion thermal forces are typically negligible. The force density acting on the ion species is thus given strictly by

$$\vec{F}_i = Zqn_i\vec{E}, \tag{3}$$

where $\vec{E}$ is the local electric field, q is the fundamental charge, Z is the charge state of the ions, and n_i is the ion density. Ion acceleration processes in turn are differentiated by the mechanism that provides this electric field. With this in mind, we describe in the following section common figures of merit for ion acceleration and then assess these metrics for several methods for acceleration.

3.2. Figures of merit

3.2.1. Current density. The current density produced by an ion source is denoted as

$$j_i = \frac{I_i}{A_i}, \tag{4}$$

where A_i is the cross-sectional area of the accelerated ion beam. This area often is equivalent to the exit area as shown in figure 1. The current density is a proxy for the flux of particles incident on a surface. This is a key parameter for in-space propulsion applications where higher flux corresponds to a smaller cross-sectional area to generate thrust. This is a major consideration for minimizing the size of the propulsion subsystem on a spacecraft. Similarly, the flux is critical for materials processing applications where larger values can translate into faster sputtering or etching rates.

3.2.2. Ion energy. The second performance metric for ion acceleration is the average ion kinetic energy generated by the system:

$$E_i = \frac{1}{2}m_i u_i^2, \tag{5}$$

where u_i is the average ion velocity after exiting the acceleration stage. The energy of the beam is directly correlated with the speed of exhaust. For propulsion applications, this is a critical factor that relates to the specific impulse, I_{sp},which is a measure of the propellant efficiency. Formally, the specific impulse for a device that provides constant thrust is defined as $I_{\mathrm{sp}} = \frac{1}{g_0}\frac{T}{\dot{m}}$ where T is thrust $\dot{m}$ is mass flow rate, and g_0 is the acceleration of gravity at sea level. For systems with a high degree of mass utilization and monoenergetic beams, the specific impulse scales with the ion velocity, $I_{sp} = u_i/\,g_0$. Beyond propulsion, the directed energy, E_i, is also an important metric governing the degree of sputtering and etching for materials processing applications.

3.2.3. Energy spread. The energy spread is an indication of how mono-energetic the ion beam is after acceleration. We represent this spread as

$$\langle \sigma_E \rangle , \tag{6}$$

which has units of energy. This parameter can be interpreted as a proxy for the kinetic definition of ion temperature, though in many applications the actual thermal heating of the ions is negligible. Rather, the energy spread captures the fact that the acceleration process may not act on all sourced ions in the same way, leading to a distribution in energy for the accelerated beam. This variance can impact the efficiency of propulsion systems as well as the accuracy and precision in etching processes.

3.2.4. Acceleration efficiency. This metric quantifies the ratio of energy required to accelerate the ions, E_{in}, versus the amount of energy the ions achieve after acceleration, E_i, in the desired direction. This is denoted as

$$\eta_{\text{accel}} = \frac{E_i}{E_{\text{in}}}. \tag{7}$$

Multiple factors can influence the acceleration efficiency. For example, it decreases if not all accelerating electric field is oriented in the desired direction. Similarly, if ionization occurs during acceleration, ions born at different locations in the acceleration field will obtain different final energies. This is manifest both as increased energy spread and lower acceleration efficiency.

3.3. Types of acceleration processes

3.3.1. Gridded acceleration. Conceptually, the simplest mechanism for accelerating ions generated by a source is with a series of biased grids (figure 3). In this case, the ions are extracted into the space between two parallel grids. An electric bias, V_b, is applied between these grids, leading to an approximately uniform electric field. This field accelerates the ions electrostatically through the gap where they then pass through the holes in the downstream grid.

There are several advantages for the gridded ion acceleration method. First, there is a high degree of versatility in controlling the speed of the ions. From energy conservation, the kinetic energy of emerging ions is $E_i = ZqV_b$. The incident energy of ions thus can be changed by adjusting the bias voltage. Second, since ions enter the grids from the upstream plasma generator with relatively low kinetic energy, the generated beam is nearly monoenergetic, i.e. $\langle \sigma_E \rangle / E_i \ll 1$. This is an enabling feature for applications where precise control of the properties of the beam is a key requirement. Third, the generated beam is relatively well collimated such that the acceleration efficiency, η_{accel}, approaches unity.

The major drawback of gridded acceleration stems from the so-called space charge limit. Only a single polarity of charge species can enter the gap, and as the number of ions increases, the combined electric field from these charges begins to oppose and ultimately nullify the applied field near the upstream grid. This places an upper bound on the current density of ions that can be extracted and accelerated through the gap for a given applied voltage and grid spacing (see [2]). This limit is given by the Child-Langmuir law:

$$j_i^* = \frac{4\epsilon_0}{9}\sqrt{\frac{2q}{m_i}}\frac{V_b^{3/2}}{d^2}, \tag{8}$$

where ϵ_0 is the permittivity of free space and d is the distance between the grids. This upper bound on current density can limit the thrust density (thrust per exit area) of some propulsion concepts. Similarly, this limit also in principle can be problematic for applications requiring high flux densities for the sputtering or etching of materials. The space charge limit can be defeated by employing smaller gaps between the grids, but this may result in arcing [2].

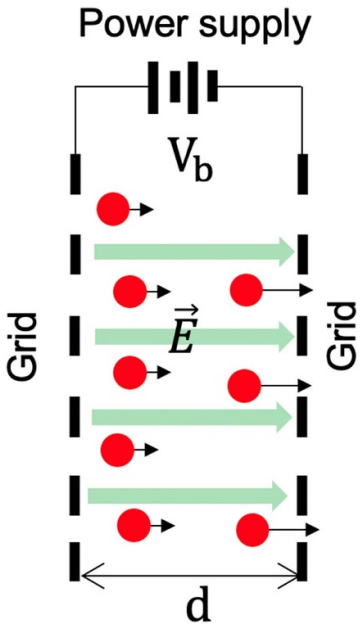

Figure 3. Illustration of gridded ion acceleration. where red spheres denote positively charged ions.

3.3.2. Crossed-field, electrostatic acceleration. Figure 4 shows a canonical illustration of a crossed-field accelerator. In this device, an electric field, $\vec{E}$, is produced by a potential difference applied across a confining magnetic field, $\vec{B}$. Both charge carriers—ions and electrons—are in the device, but the magnetic field is tailored such that only the electrons are subject to a non-negligible magnetic component of the Lorentz force. This is accomplished by ensuring that the characteristic length scale of the system lies between the Larmor radii of the two species, $r_{l(e)} < L < r_{l(i)}$. The crossed field configuration drives the magnetized electrons into a drift in the $E \times B$ direction, preventing this species from following the applied electric field. This impediment to cross-field transport

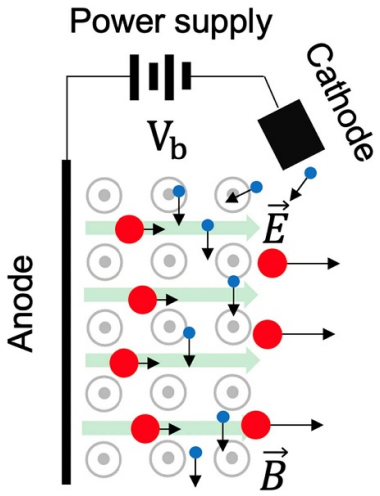

Figure 4. Illustration of canonical geometry for a cross-field accelerator with ions (red) and electrons (blue).

is necessary, as otherwise the electron current would dominate the power consumption of the bias supply. The ions, which are unmagnetized, only respond to the applied electric field and are accelerated by the electrostatic force (equation (3)). As with gridded ion thrusters, the gain in ion kinetic energy is approximately $E_i = ZqV_b$.

The major advantage of the crossed-field device in contrast to a gridded accelerator is that the acceleration process is quasi-neutral. On average, the electric fields from the charge carriers of each species cancel, thus eliminating the problem of space charge build-up and enabling higher current density, j_i. This feature can be leveraged to generate higher thrust levels for a given cross-sectional area or to provide more fluence to a sputtering target. With that said, the available current density is not unlimited as there is some empirical evidence (see [11, 12]) to suggest that with uncommonly high levels of current density, the plasma confinement in the $E \times B$ drift can be adversely impacted. This can decrease the overall efficiency of the device. We note as well that with increasing magnetic field strength, the ions become magnetized, i.e. $r_{l(e)}, r_{l(i)} < L$. In this case, this heavier species is forced into a similar $E \times B$ drift as the electrons, preventing cross-field acceleration. Partial magnetization is thus critical to the efficient operation of these devices.

With respect to disadvantages of this acceleration process, since the electric field is typically not as collimated in crossed-field devices, the ion plume can have a larger divergence than in gridded ion accelerators. This can lower the efficiency of thrust generation for applications related to propulsion and can adversely impact the precision of materials processes that requires a focused beam. Additionally, many $E \times B$ configurations combine both the generator and accelerator into one stage. In this case, ions can be created at multiple initial potential values within the domain, thus resulting in a beam with higher degree of energy spread, $\langle \sigma_E \rangle$. This so-called polydispersive effect also impacts the acceleration efficiency for crossed-field thrusters, η_{accel}, as on average, not all the applied potential is used to accelerate the ions, i.e. $E_i < \text{ZqV}_\text{b}$. Acceleration efficiencies thus are typically lower than 95%. A related factor impacting the acceleration efficiency is the spatial distribution of the potential downstream of the anode. This stems from how the electrostatic circuit is completed. For example, if a cathode is employed to terminate the electric field (figure 4), some of the applied voltage will be expended in extracting electrons from this source rather than accelerating the ions.

3.3.3. Ambipolar acceleration. In the ambipolar acceleration process, the electric field to accelerate the ions is not applied directly. Rather, this force stems from an ambipolar field generated indirectly though the action of a thermal pressure gradient established by the electrons. This process is shown qualitatively in figure 5. In this case, a parallel, diverging magnetic field is applied to a quasi-neutral plasma. The electrons in the plasma, which are more mobile than the ions by virtue of their hotter temperatures and smaller mass, diffuse out of the volume along the expanding magnetic field. This process gives rise to a disparity in charge between the downstream electrons and the remaining ions in the source. The charge imbalance in turn leads to an electric field, the so-called ambipolar field, that accelerates the ions with the electrons, ultimately maintaining a quasi-neutral and globally current-free system.

A simple model for this process is given by assuming the electron dynamics parallel to the field lines are collisionless and that electron inertia can be neglected. In this case, the ambipolar electric field accelerating the ions scales as

$$\vec{E} = -\frac{1}{qn_e}\nabla P_e, \tag{9}$$

where P_e denotes the electron pressure and n_e is the electron density. This expression shows that the accelerating electric field on the ions arises from the electron pressure gradient. In order to relate this ambipolar acceleration to the ion energy, it is common (see [13–15]) to assume an equation of state for the plasma density (though we note more sophisticated methods account for the kinetic distribution of electrons during expansion [16, 17]). This law takes the form, $T_e n_e^{1-\gamma} = \text{const.}$ where γ is the polytropic index and T_e is the electron temperature. Classically, the polytropic index can assume values from $\gamma = 1$ (isothermal electrons) to $\gamma = 5/3$ (adiabatic electrons). In practice, the measured values typically fall between these limits.

Provided the accelerating electric field is time-invariant, we can employ the electrostatic approximation combined with the equation of state to find the ion kinetic energy after ambipolar acceleration:

$$E_i = Z\frac{\gamma}{\gamma - 1}T_e^{\text{in}}\left(1 - \frac{T_e^e}{T_e^{\text{in}}}\right), \tag{10}$$

where T_e^{in} and T_e^e denote the electron temperatures before and after acceleration respectively. This result underscores the fact

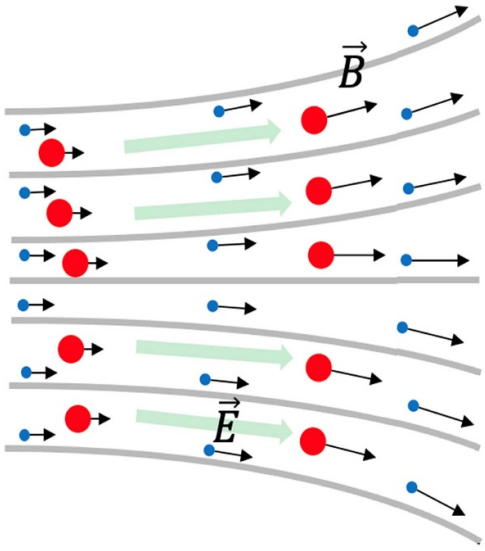

Figure 5. Illustration of ambipolar acceleration where expansion of magnetized electrons (blue) along a confining magnetic field results in an ambipolar electrical field that accelerates ions (red).

that the ambipolar acceleration process is inherently thermal [8], depending on the change of electron temperature that results from expansion. This is analogous to conventional rocket nozzles where combustion products are heated and then expanded through a variable cross-section nozzle. However, unlike in conventional nozzles where thermal limits on the wall materials preclude the ability to achieve temperatures much higher than 3000 °C, the electron temperatures can be orders of magnitude higher in a low-pressure ambipolar accelerator [9]. The ability to accommodate these higher temperatures stems in part from strong magnetic fields in these systems which help limit thermal flux to the walls.

As with the crossed-field accelerators, a major advantage of the ambipolar acceleration process is that it is quasi-neutral. It therefore does not have, in principle, an upper bound on current density from space charge limitations. A second major advantage is that the electrons can be heated through indirect means, e.g. by injecting microwave or RF energy. Thus, the acceleration can be achieved without relying on the direct use of electrodes immersed in the plasma. This prolongs the life of the system as wear on the accelerating structures due to plasma bombardment is mitigated.

With that said, one of the major challenges with ambipolar accelerators is that electron temperatures to achieve comparable ion energies to electrostatic acceleration can be high, e.g. >50 eV. Imparting this degree of heating efficiently has proved to be problematic to date, though recent results using ECR heating have exhibited ion energies comparable to electrostatic acceleration schemes [8, 18]. Similarly, as with crossed field accelerators, since ions are created at different spatial locations and potentials in the accelerator, these devices can be subject to a high degree of variance in the beam energy, leading to higher values of $\langle \sigma_E \rangle$ and lower average values of E_i.

As a last comment, as equation (10) shows, the kinetic energy of the ions depends on the difference in electron temperature before and after expansion. If expansion is not complete, there is some residual thermal energy. This can lead to an effective decrease in acceleration efficiency, η_{accel}. With that said, there is ambiguity about the value of the electron temperature after expansion, T_e^e, which stems from the question of where the field-guided plasma expansion stops and the plasma 'detaches' from the expanding magnetic field (see [19]). The assumption $T_e^e \rightarrow 0$ can be invoked to provide an estimate for the maximum accelerating potential that can exist. Alternatively, in lieu of a fluid interpretation, previous work has invoked assumptions about the shape of the kinetic distributions of electrons at the exit plane [8]. By assuming a truncated Maxwellian and enforcing a current-free approximation, it is possible to relate the accelerating potential exclusively to the electron temperature at the exit plane, T_e^{in}. In this case, the accelerating energy has the same form as equation (10), but $T_e^e \rightarrow 0$ and the polytropic index depends on the ratio of ion to electron mass.

3.3.4. Lorentz acceleration. Figure 6 shows a notional geometry for 'self-field' Lorentz ion acceleration at steady state. As with ambipolar acceleration, in low-temperature, partially magnetized plasmas, the Lorentz acceleration is provided indirectly by the electrons [20]. A current density, $\vec{j}_e$, carried primarily by electron motion through a central electrode, induces a magnetic force in the azimuthal direction. This current is then emitted from a cathode and drawn radially toward a collecting anode. The Lorentz force between the induced magnetic field and current leads to an acceleration of the electrons in the crossed field direction. This preferential acceleration of the electrons gives rise to a charge disparity. The resulting induced electric field can be approximated from a collisionless generalized Ohm's law:

$$\vec{E} = \frac{1}{qn_e}\left(\vec{j}_e \times \vec{B}\right), \tag{11}$$

where we have neglected the pressure gradient contributions. This field then accelerates the ions per equation (3). This self-field Lorentz force can be further augmented by adding additional external sources of magnetic field, e.g. in the form of a concentric solenoid. This is termed an 'applied field' configuration [21].

Lorentz force acceleration is a quasi-neutral process and therefore can support higher current densities than space-charged limited acceleration. Moreover, unlike in the crossed-field configuration, which relies on the ability to trap electrons in a drift, the Lorentz force depends explicitly on the cross-field motion of electrons. As a result, in principle, this system does not have the same collisionally induced limits in current density anticipated for crossed-field devices [22]. Indeed, Lorentz acceleration can support the highest current densities of the concepts discussed in this article. Moreover, Lorentz acceleration occurs even in the limit when ions become magnetized. This stems from the fact that the ion

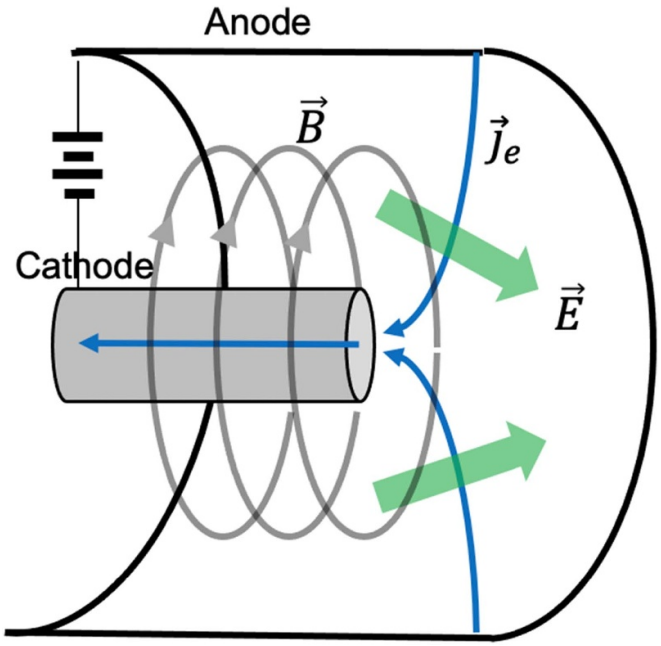

Figure 6. Illustration of steady-state Lorentz force acceleration for ions in a partially magnetized, cylindrically symmetric plasma.

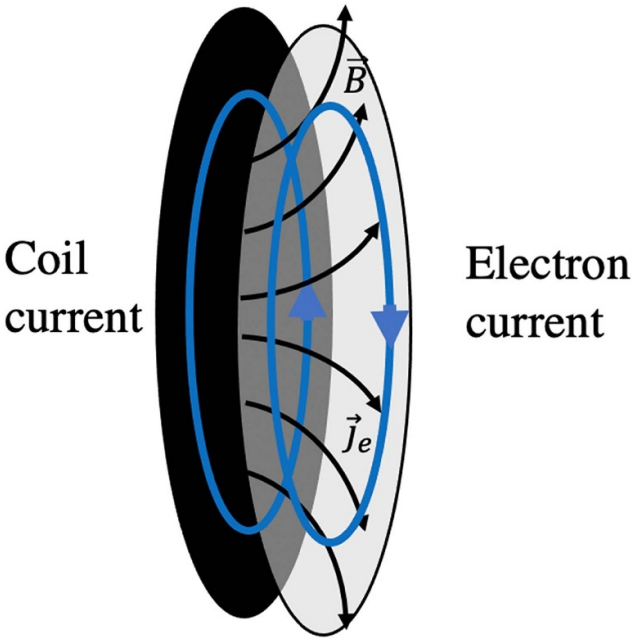

Figure 7. Illustration of a pulsed inductive Lorentz acceleration process.

Lorentz force in this system acts in the same direction as for the electrons.

In terms of performance metrics, the kinetic energy of ions in the Lorentz acceleration can be estimated from a collisionless momentum equation:

$$E_i = \frac{m_i}{2}\left(\frac{1}{\dot{m}_i}\int_V \left(\vec{j}_e \times \vec{B}\right) dV\right)^2, \tag{12}$$

where the integral is performed over the entire plasma volume and $\dot{m}_i$ is the mass flow rate of ions into the volume. This ion flow rate can be related to the total mass flow rate through the beam utilization efficiency (equation (1)). Equation (12) indicates that the achievable ion energy in the Lorentz force accelerator is a result of a volumetric body force. The magnitude can be adjusted by lowering the inlet flow rate or increasing the electron current.

To this latter point, in the self-field mode, the generated magnetic field also scales with the electron current density such that $E_i \sim I_e^2$ where I_e is the total electron current. This relationship indicates that the degree of Lorentz acceleration can be tailored by increasing the current in the system. In practice, however, achieving the high current densities necessary for efficient operation in steady-state can be a challenge—particularly for the lifetime of the electrodes employed to maintain the discharge.

With this in mind, pulsed systems are also employed for Lorentz acceleration [23]. Figure 7 shows this process qualitatively. In this case, current is pulsed in a coil adjacent to the plasma in the azimuthal direction. This results in a magnetic field directed approximately radially along the plasma. At the same time, the coil current induces a mirror current in the plasma in the azimuthal direction. The resulting Lorentz force between the plasma current and coil magnetic field accelerates the electrons through the Lorentz force, dragging the ions with them through the induced electric field that results from the charge disparity.

Pulsed acceleration schemes have two major advantages over steady-state Lorentz accelerators. The first is that it is possible to transiently induce larger currents, thereby leading to higher achievable ion kinetic energy (equation (12)). The second is that since these systems rely on induction, they can be constructed such that the plasma has minimal contact with the electrodes. This enables operation on more reactive gases that otherwise would corrode the components in gridded or cross-field accelerators.

As with crossed field devices, Lorentz force accelerators often have ionization and acceleration occur in the same region, which can lead to dispersion in the energies of the accelerated species. This results in larger energy spread, $\langle \sigma_E \rangle$, and reduced acceleration efficiency, η_{acc}.

3.3.5. AC acceleration. The previous sections treated ion acceleration in DC fields. However, ion acceleration can also occur in AC fields. This process offers several potential advantages over DC devices related to plasma production, plasma uniformity, and charge neutralization. Figure 8 shows a notional schematic for this acceleration process where a sinusoidal voltage waveform is applied across a set of electrodes of two different sizes. While this may appear to be unsuitable for effective ion acceleration since the time-averaged voltage is zero, the large disparity in electron and ion masses in a plasma causes a self-consistent DC self-bias to be produced across each electrode-plasma sheath. In this

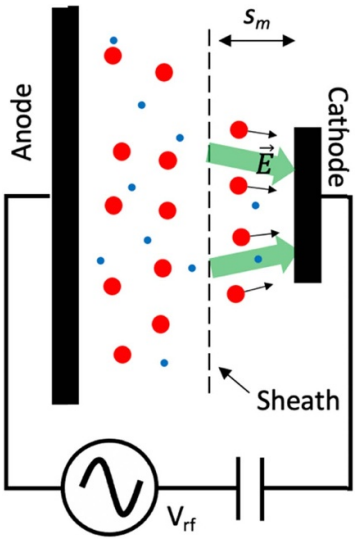

Figure 8. Schematic of AC acceleration based on asymmetric electrodes. Note that the sheath on the anode side is not shown as the dominant DC potential drop occurs on the cathode.

sense, the applied AC waveform generates a high-voltage virtual electrode in front of each physical electrode. If the applied AC frequency (typically in the RF range) is high enough, ions cannot respond to the instantaneous time-varying electric fields and see only a time-average field leading to strong acceleration.

The dynamics of the plasma sheath in an AC device are essential to ion acceleration. While a full description of these processes is complex and non-linear, the formation of a self-bias field can be illustrated with a simple example. Sheaths can be modelled as capacitors and since capacitance is proportional to area, the sheath in front of the larger electrode will have a higher capacitance. When considering the sheaths at both electrodes together, a capacitive voltage divider is produced in the discharge with most of the applied voltage dropped across the smaller electrode [3]. We then consider a single-frequency sinusoidal voltage waveform, $V_{\mathrm{rf}}\sin\omega t$, applied to a discharge where one of the electrodes is much smaller than the other. If the AC frequency is high enough, the ion motion is not strongly modulated while the electron flux is. The ion flux thus can be treated as Bohm-like into the sheath while the electron sheath is modified by the varying sheath potential. Ensuring charge balance through the circuit leads to an average bias voltage that accelerates the ions, resulting in a kinetic energy of:

$$E_i = ZT_e\left\{\frac{1}{2}\ln\left(\frac{m_i}{2\pi m_e}\right)+\ln\left[I_0\left(\frac{V_{\mathrm{rf}}}{T_e}\right)\right]\right\}, \tag{13}$$

where m_e is the electron mass and I_0 is the zeroth order modified Bessel function of the first kind. The first term in equation (13) is the usual floating potential of a DC plasma sheath, while the second term represents the effect of the applied AC voltage which adds a significant offset. In fact, for $V_{\mathrm{rf}} \gg T_e$, $E_i \approx ZV_{\mathrm{rf}}$.

This result underscores the fact that the average kinetic energy of ions can be controlled in these systems by varying the amplitude of the applied RF field. With that said, in real discharges, not all the voltage drop occurs across a single AC sheath, and the time-varying sheath voltage may be non-sinusoidal. This leads to decreases in the effective acceleration efficiency, η_{accel}. These higher order effects can be treated with more complete and sophisticated AC sheath models (see [24–26]).

As with gridded acceleration, the AC process is not quasi-neutral. This is because it occurs predominantly through the sheath that forms at the boundary of the electrode where there is a disparity in local electron and ion densities. Unlike in the gridded thruster where only one charge species is present, however, the sheath does have both electrons and ions, and the electrons partially compensate the ion space charge in the sheath. This leads to a modified Child-Langmuir law for the ion current density [3, 6]:

$$j_i = K_i\epsilon_0\sqrt{\frac{2q}{m_i}}\frac{\bar{V}^{3/2}}{s_m^2}, \tag{14}$$

where s_m is the maximum sheath width, $\bar{V}$ is the time-averaged sheath voltage, and K_i is a numerical factor. The maximum sheath width is [3, 6]

$$s_m = K_m\lambda_{\mathrm{De}}\left(\frac{\bar{V}}{T_e}\right)^{3/4}, \tag{15}$$

with $K_{m,}$ a numerical factor and $\lambda_{\mathrm{De},}$ the electron Debye length. For a single-frequency discharge with equal area electrodes, $K_i \approx 1.05$, $\bar{V} \approx 0.42V_{\mathrm{rf}}$, and $K_m \approx 1.22$ [24, 25]. In this case, the AC space-charge limited ion current density is almost two times higher than the DC space-charge limit. In practice, this suggests that even though the AC acceleration scheme is space charge limited, it can achieve higher ions fluxes than the gridded acceleration process.

Given the oscillatory nature of the applied AC waveform, the variance in ion energy, $\langle\sigma_E\rangle$, can be relatively large for this acceleration scheme when contrasted with the other accelerating processes. Indeed, depending on the applied AC waveform, the operating pressure, and the area of the electrodes, complicated ion flux distribution functions (IFDFs) can be produced at the electrodes [3, 6, 27, 28]. These IFDFs represent the superposition of several processes including ionization within the sheath region, ion-neutral collisions, and AC modulation if the ion transit time is comparable to or less than the AC period. Example IFDFs for a dual-frequency discharge are shown in figure 9 [27]. The resulting ion distributions are very broad and show a large variance, $\langle\sigma_E\rangle$. The average ion energy, E_i, is obtained through moments of the distribution and is typically less than the energy of the main peak because of the contribution of lower energy ions.

4. Plasma diagnostics

As we have outlined in the preceding sections, there are several approaches for creating and accelerating ions in low

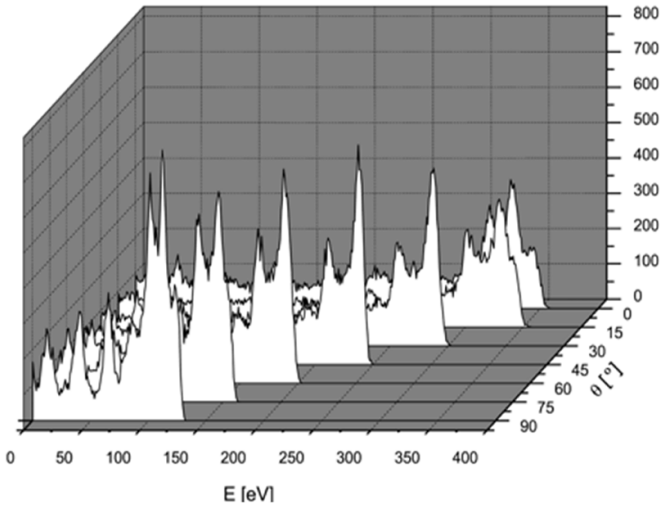

Figure 9. Ion flux distribution functions at each electrode in a dual-frequency (13.56 MHz and 27.12 MHz) discharge as a function of the phase angle between applied frequencies in a low-pressure argon discharge. Reproduced from [27]. © IOP Publishing Ltd. All rights reserved.

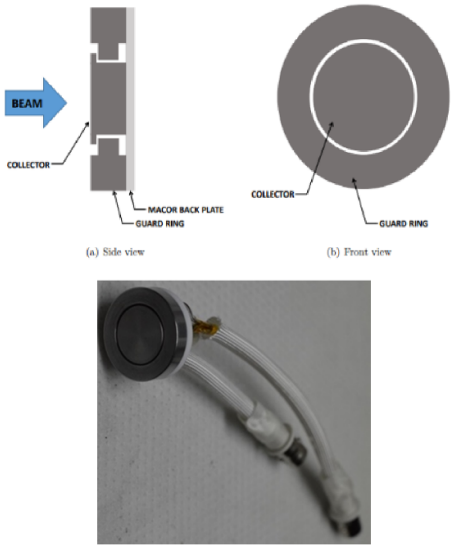

Figure 10. Schematic and image of a Faraday probe employed for ion current density measurements.

temperature sources. In turn, there are key metrics for evaluating their performance including the ion production cost, mass utilization, mean kinetic energy, energy spread, and acceleration efficiency. These aspects of operation are typically inferred with probe-based or optical plasma diagnostics inserted. We outline in the following commonly employed diagnostics, their principles of operation, and key information they yield regarding device operation.

4.1. Mass utilization

The Faraday probe is the most common method for inferring mass utilization. Figure 10 shows a schematic of a typical form of this diagnostic along with an image. A more detailed description of this system as well as best practices for implementation and data analysis can be found in [29].

The Faraday probe is electrically biased negatively with respect to the local plasma potential to the point that it repels nearly all electrons and only collects ions. By orienting the probe toward the ion source, the amount of collected current on the probe provides a proxy for the local ion current density, which can be inferred by dividing the measured current by the probe area. This probe is typically scanned across the exit of the discharge to yield a spatial measurement of the current density of the plume (figure 11).

By integrating azimuthally (typically by invoking arguments from the symmetry of the system), the total ion current, I_i, produced by the system can be estimated. Since the flow rate is a design parameter and is thus known, the mass utilization efficiency thus can be calculated from equation (1). We note that if there are multiple charge states, this calculation must be modified by a factor that accounts for these contributions [2]. The relative charge fraction can be estimated with an $E \times B$ probe (See section 4.2.2).

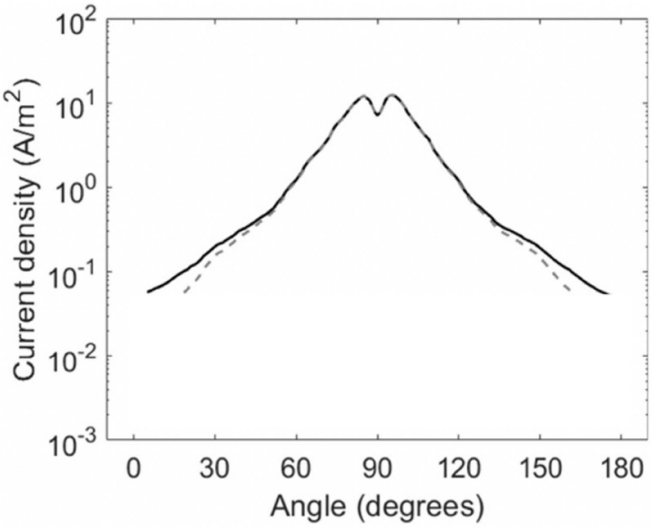

Figure 11. Ion current density trace as a function of angle from the centerline of a Hall effect thruster at a location 1 m downstream of the thruster. Reprinted from [30], with the permission of AIP Publishing.

4.2. Energetic properties of the plume

As described in section 3.2, the properties of the accelerated ions—particularly the mean ion energy and spread—are key metrics for evaluating the performance of these systems. To this end, several diagnostics are employed to characterize these properties.

4.2.1. Retarding potential analyzer. The retarding potential analyzer (RPA) is one of the most widely used diagnostics for assessing the ion energy distribution in low temperature ion sources [31]. Figure 12 shows a schematic of this probe as well as its principle of operation. The system is comprised of a series of grids electrostatically biased to different potentials.

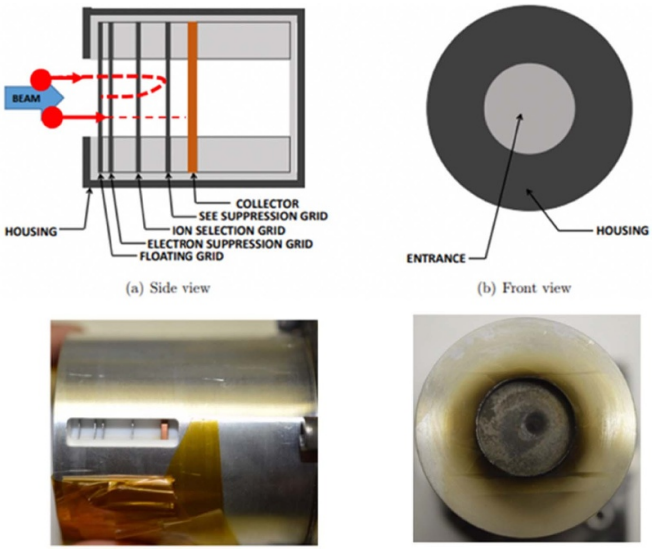

Figure 12. Schematic and images of a RPA.

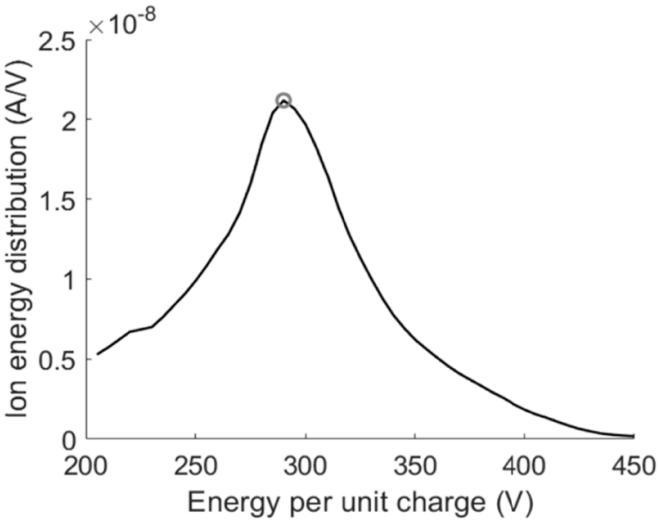

Figure 13. Example distribution function of ion energy per unit charge in the plume of a Hall effect thruster. Reprinted from [30], with the permission of AIP Publishing.

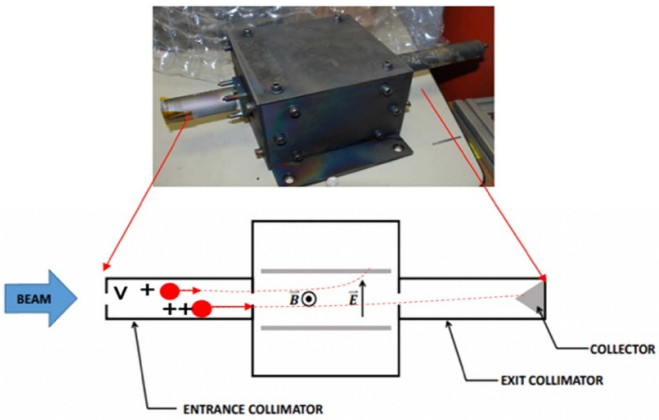

Figure 14. $E \times B$ probe schematic and image illustrating the principle of operation.

The grid closest to the plasma is typically floating or biased negatively with respect to the plasma. This serves to screen electrons from entering the diagnostic while allowing ions to pass. The next set of grids apply a bias voltage to decelerate the ions. The fraction of ion population with energy exceeding this bias then transits through this potential barrier and is collected onto the plate. A fourth grid between the selection grid and the collector serves to suppress secondary electrons generated by ion impact on this plate.

The signal collected at a given bias voltage is proportional to the total ion energy distribution in the plume. By varying the potential from low to high values, fewer ions are collected, and the entire distribution is mapped. Differentiating this trace with respect to the applied voltage yields the ion velocity distribution function expressed in units of energy per charge (figure 13). The distribution in turn provides a quantitative assessment of both the most probable kinetic energy (typically correlated with the mean kinetic energy) as well as the energy spread (represented by the relative width of the distribution).

The results of RPA analysis are caveated by the fact that the distribution represents the ion energy per unit charge and thus cannot disambiguate different charge states. Similarly, instrument broadening associated with the geometry of the probe, non-uniformities in the incident plasma, and build-up of back pressure in the diagnostic can introduce anomalous spreading in the distribution. Techniques for the design and mitigation of these effects are discussed in more detail in [31, 32].

4.2.2. $E \times B$ probes. The relative distribution of charge states can impact the average kinetic energy as well as mass utilization of the source. Similarly, the presence of multiple charged species can lead to effective broadening in the ion energy distribution. With this in mind, the $E\times B$ probe (alternatively called the Wien probe) is a tool for characterizing the relative distribution of ion charges states in the ion source. Figure 14 shows a simplified schematic for this diagnostic along with the principle of operation. A small orifice is employed at the entrance to the probe to reduce the relative flux of ions into the diagnostic. A strong magnetic field is then established by a permanent magnet transverse to the direction of travel while an electric field is oriented orthogonal to both the probe axis and magnetic field. This is generated by an applied voltage across the narrow gap. The geometry terminates in a collector plate that measures the incident current.

The magnetic field in the probe is sufficiently strong that the ion trajectory is influenced by the magnetic component of the Lorentz force. As a result, if the electric and magnetic fields of the Lorentz force are not equal and opposite, the ion trajectory will be curved, and the inlet ions will not impact the collector plate. By tailoring the electric field to cancel the Lorentz force, the diagnostic thus acts as an effective gate. For a given applied electric field, the ions able to intercept the collector are dictated by the incident velocity.

By sweeping across applied voltage, the relative distribution of the component of ion velocity normal to the probe surface can be inferred. The ability to determine charge state in turn stems from the assumption that the acceleration process

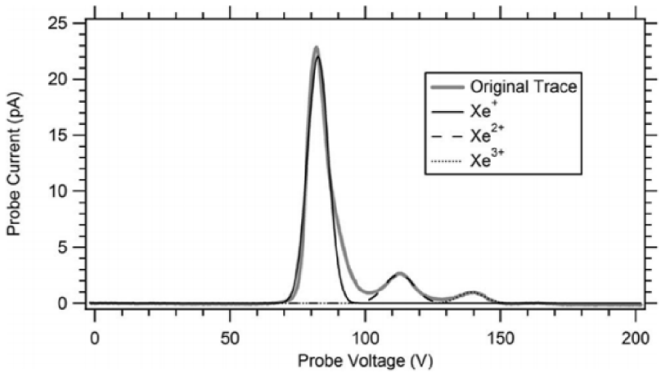

Figure 15. Example of $E \times B$ spectrum showing charge state for an operating on xenon. The original trace corresponds to the raw data while the lines correspond to numerical fits to represent the relative fraction in each charge state. Singly, doubly, and triply charged states are shown.

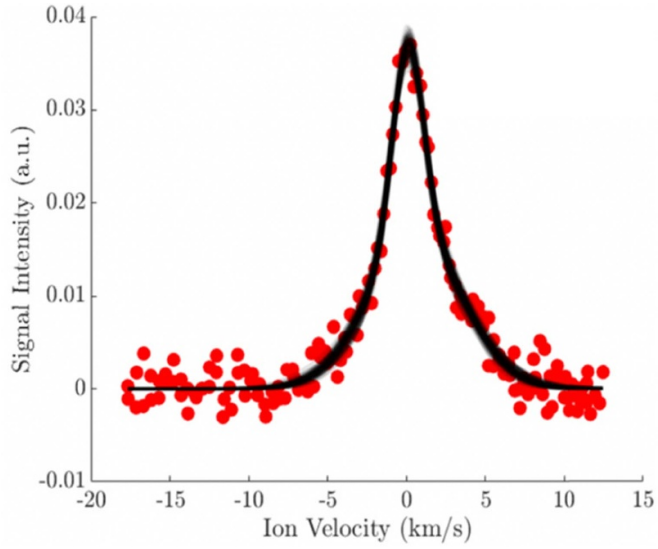

Figure 16. Ion velocity distribution function inferred from LIF. Reproduced with permission from [35].

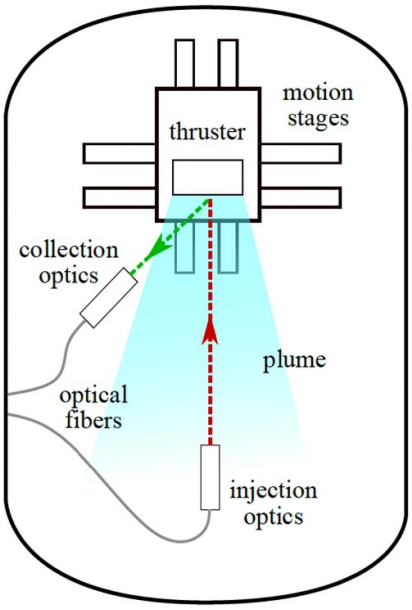

Figure 17. Image of a LIF system arranged with respect to an ion source discharging into a vacuum facility. Reproduced with permission from [35].

is electrostatic. Thus, for a given electric field in the ion accelerator, the velocities of different charge states will differ by a factor of $\sqrt{Zq}$. Figure 15 shows a typical trace generated from an $E \times B$ probe from a crossed-field discharge. Each peak represents a different charge state where greater charge corresponds to a higher required probe voltage/electric field. The total relative fraction of ion current for charge state is in turn inferred by integrating under the curve of each peak. With that said, there are several sources of systematic bias—particularly instrument broadening—that can introduce error to this integration. Reference [33] provides guidance on different strategies to deconvolve these effects.

4.2.3. Laser induced fluorescence. Laser induced fluorescence (LIF) is another widely employed method for inferring the ion velocity distribution function in the plasma (see [34]). In this scheme (figure 17) collimated laser light tuned to an excitation line of the ion population of interest is injected into the plasma. If the local ion population has a relative drift with respect to the beam direction, the frequency of the laser light in the ion frame of reference is Doppler shifted. To excite ions moving at a particular speed, the laser light must therefore be tuned to compensate for the Doppler effect. Once the transition is excited, the state rapidly decays to a lower energy, emitting light. In non-resonant schemes (the simplest to perform for light detection), the emitted light is at a different wavelength than the incident light, and the relative intensity of this emitted signal scales with the density of ions moving at the Doppler-shifted speed with respect to the beam. By sweeping across wavelength and measuring the intensity of the signal, it is possible to generate velocity distributions of the component of velocity parallel to the laser beam direction. Figure 16 shows an example of the results inferred from an LIF measurement.

The LIF method has two major advantages compared to probe-based electrostatic energy probes like RPAs. First, it is non-invasive. Unlike RPAs, LIF systems do not have active probing elements in the plasma. This is a critical advantage as probes have been shown to actively perturb discharges [36, 37]. The second advantage is that this methodology can have higher spatial resolution. This resolution is based on the overlap of the injected laser beam and the collection cone of the optic that is employed to detect the emitted light stimulated by the incident light (figure 17). This volume can be tailored to be less than 1 mm in diameter, an order of magnitude smaller than common RPA designs.

While LIF is increasingly becoming a staple diagnostic for plasma-based ion sources, this technique does have some limitations. For example, each LIF injection scheme is targeted to only one charge state, typically singly charged. The velocity distribution of the higher charge states is thus unknown. Similarly, the most common version of this method as applied to ion sources only targets a metastable state of the ion

population. This stems from the fact that the required laser wavelength to excite the ground state requires ultraviolet lasers that are prohibitively expensive. Thus, the signal generated by the standard method only represents a subpopulation of collisionally-excited ions. This metastable population is mapped to all the ions by assuming they are in equilibrium. This assumption can be problematic—particularly for trying to apply LIF schemes to measure time-resolved behavior in the ion dynamics [38]. With that said, resonant two-photon excitation techniques have recently emerged as an alternative to overcome this limitation, as these schemes can directly excite the ground state of the ions of interests [39].

A second limitation stems from the low signal-to-noise ratio of LIF. The emitted signal from the induced fluorescence is several orders of magnitude lower than the ambient light generated by the plasma. As a result, signal-to-noise reduction techniques like lock-in amplification must be employed. This can be time-intensive and ultimately still results in ambiguity regarding the low-amplitude tails of the velocity distributions.

4.3. Species composition

For some ion source applications that involve etching or surface material sputtering, more complex molecules are used in the working gas. These can lead to a wide range of dissociated species and different charge states. At the same time, residual gas in vacuum chambers where the ion sources are employed can also introduce impurities in the discharge, which can adversely impact operation. Faced with these challenges, it is typical to employ mass spectrometers to characterize the distribution of species. The quadrupole-based spectrometer is a common tool applied for this purpose (see [40]). It yields plots of the relative species concentration as a function of particle mass.

4.4. Sputtering deposition

By design, some ion sources are employed to sputter or etch target materials. Other ion sources incidentally sputter material from the surrounding environment when the generated beam intercepts the walls of the test facility. In both cases, it is often necessary to characterize the degree of sputter. This commonly is performed with a quartz crystal microbalance [41, 42]. In effect, these sensors are comprised of an underlying substrate that resonates at a given frequency. As mass from the sputtered environment or target accumulates on the sensor, the resonant frequency changes. Measurements in this change can be leveraged to infer both differential and total deposition from the facility.

4.5. Plasma density and temperature

Langmuir probes (LPs) are the most common tools used to measure the plasma density, electron temperature, plasma potential, and the electron energy probability function (EEPF) or electron energy distribution function. They consist of a small, biased metal probe tip immersed in a plasma that collects a current of electrons and ions. This current is typically determined by measuring the voltage drop across a known sense resistor in the probe electrical circuit external to the plasma. By sweeping the applied bias voltage and measuring the corresponding current, a current–voltage (*IV*) curve is obtained [43]. This *IV* curve (figure 18) is then analyzed using standard probe theories to extract important plasma information.

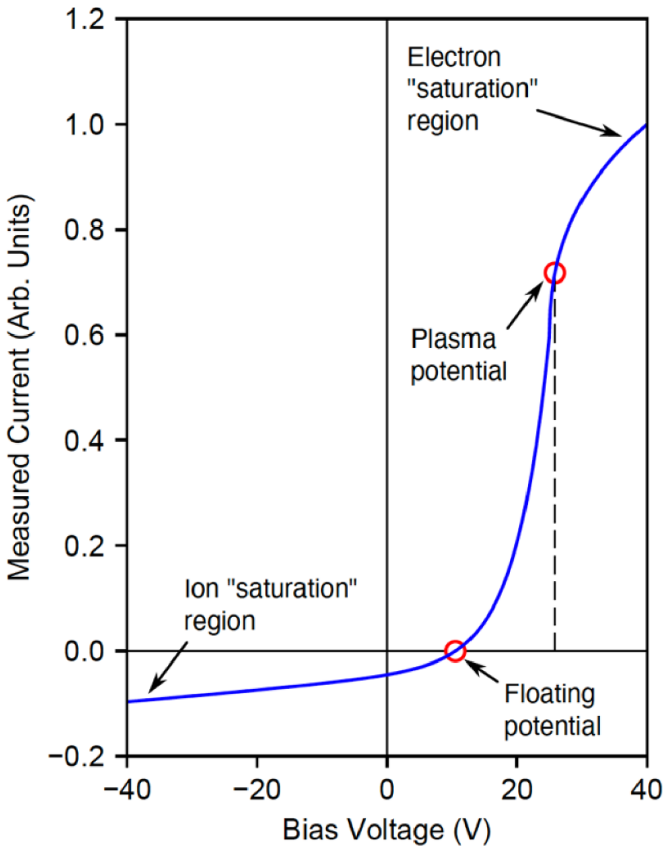

Figure 18. Example of a typical langmuir probe IV curve illustrating key features.

Different LP designs exist which use planar, cylindrical, or spherical probe tips [3, 44]. By biasing LPs both negatively and positively, electrons and ions can be collected. For large negative biases, all electrons are repelled and only ions reach the probe tip. If the probe bias is sufficiently high, the ion current, in principle, saturates. This part of the *IV* curve is known as the ion saturation region. As the bias voltage is swept towards positive values, electrons start to be collected, and eventually a voltage is reached where the measured current is zero. This voltage is called the floating potential. For higher bias voltages, electron collection dominates until the local plasma potential is reached, after which the electron current saturates. This part of the *IV* curve is known as the electron saturation region. Because of the applied bias voltage, LPs are invasive diagnostics that can perturb the local plasma. For example, a true saturation of the electron and ion currents is typically never obtained because of the probe geometry and plasma sheath expansion as the magnitude of the bias voltage increases. This leads to a larger effective probe collecting area and a larger measured current.

Different probe theories make different assumptions concerning electron and ion collection. For example, electrons are often assumed to obey the Boltzmann relation. In this case, the slope of the natural logarithm of the probe current in the electron collection region of the *IV* curve is inversely proportional to the electron temperature [44]. The electron density can then be determined by assuming a Maxwellian flux and using the probe current at the plasma potential (which is equal to the bias voltage at which the second derivative of the *IV* curve is zero). The ion density is obtained from the ion saturation current assuming ions enter the probe sheath at the Bohm velocity, and using an appropriate model to account for sheath expansion (if the local plasma properties are such that the sheath is sufficiently large compared to the size of the probe tip itself) [43]. For cylindrical or spherical probe tips, more sophisticated models based on particle current limited by orbital motion effects exist.

An alternative probe theory that is widely used and is particularly attractive is the Druyvesteyn method [3, 6], which shows that the EEPF is directly proportional to the second derivative of the probe current with bias voltage. The electron density and temperature are then obtained by taking moments of the measured EEPF. This method is typically more accurate than other probe theories, requires fewer assumptions, and can be used to measure non-Maxwellian distribution functions. However, taking the second derivative of the *IV* curve can introduce significant numerical noise and may require filtering or the use of an analog differentiator circuit (see for example [45]). Example EEPFs measured in an ICP discharge are shown in figure 19 [46].

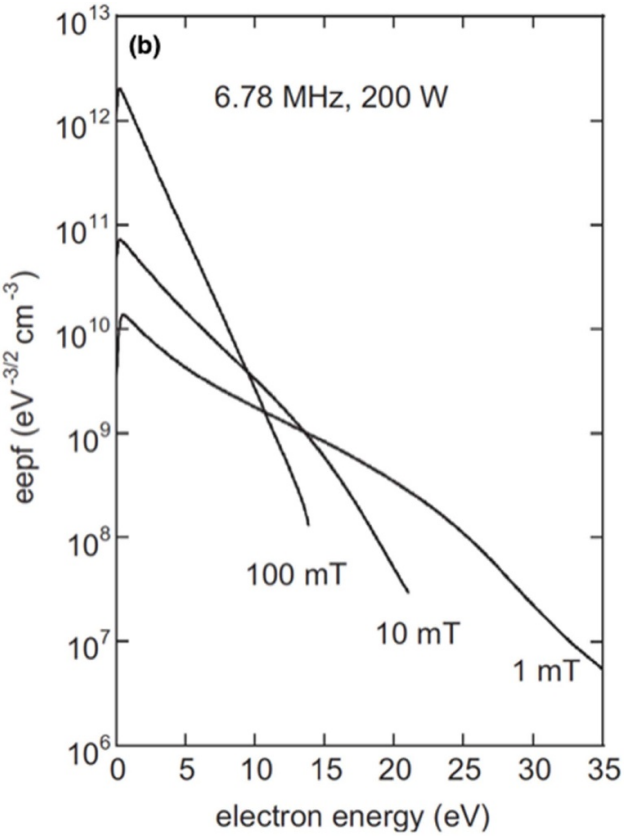

Figure 19. EEPFs at different argon gas pressures in an RF ICP. Reproduced from [46]. © IOP Publishing Ltd. All rights reserved.

The use of LPs in RF discharges requires particular care as any RF oscillations in the plasma potential can lead to a distortion of the *IV* curve. Such RF oscillations change the effective probe bias relative to the plasma and may also cause a displacement current to be collected by the probe. These effects can be reduced with RF-compensated LPs that use reference electrodes and passive circuit filters [47]. Additional LP probe design and operational considerations can be found in [48–50].

In addition to the standard LP methods, there has been recent work to apply incoherent Thomson scattering to non-invasively characterize the electron properties [51]. This method, which is based on resolving the Doppler-induced spread in light that is scattered off free electrons, is widely employed in the study of higher energy plasmas. Historically, this diagnostic technique has not translated to low temperature ion sources as the densities are too low to yield detectable signal to noise. With that said, recent innovations in filter and detection technologies have been leveraged to successfully apply this methodology to select low temperature ion sources [51, 52].

4.6. Plasma potential

The main diagnostic used to measure the plasma potential is an emissive probe, a schematic of which is shown in figure 20. Emissive probes consist of a small filament tip which emits electrons when heated to sufficiently high temperatures by an external current supply [53–55]. This tip is then usually inserted into a ceramic tube and connected to electrical wires either by silver solder, spot welding, or a tight friction fit. The external heating supply is typically isolated from ground (either with batteries or an isolation transformer) to ensure a closed heating current loop.

There are essentially two emissive probe measurement techniques: (a) The floating potential method and (b) the inflection point method. The floating potential method is by far easier and more commonly used. Here, strong electron emission from the probe tip neutralizes the positive space-charge sheath that would otherwise form around the tip [54]. Once complete neutralization occurs, the tip floats to the local plasma potential which is measured with a multimeter or oscilloscope. However, due to the strong emission required, space-charge effects can cause the probe tip to float to a slightly different potential than that of the true plasma potential. The uncertainty is typically of the order of the electron temperature [56]. Strong emission can also easily cause the filament to melt or become damaged.

The inflection point method is regarded as the more reliable and is one of the only known methods for measuring the plasma potential in a vacuum (i.e. when no plasma is present) [57]. In the inflection point method, in addition to the probe tip being heated, it is also biased. The collected current (which does not include the heating current) can then be measured as a function of the bias voltage. For biases below the plasma

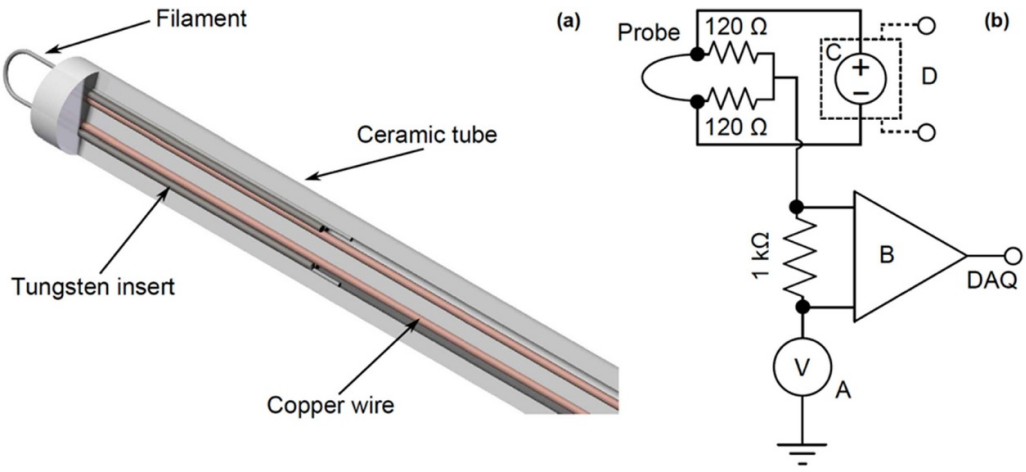

Figure 20. (a) Schematic of an emissive probe and (b) and example electrical circuit when operating an emissive probe using the inflection point method. Reproduced with permission from [59].

potential, all emitted electrons escape the probe tip, while for biases above the plasma potential, some emitted electrons are reflected and recollected by the probe. Consequently, the *IV* curve shows a strong change for biases close to the plasma potential. The plasma potential is therefore equal to the bias voltage at which the derivative of the *IV* is a maximum (i.e. the inflection point of the original *IV* curve). In practice, because of space-charge effects due to the emitted electrons, a series of *IV* curves at different electron emission currents are usually taken and the true plasma potential found by extrapolation to zero emission [57, 58].

The plasma potential can also be found using several of the other diagnostic probes discussed previously. For example, for biases above the plasma potential, the *IV* curve of a LP usually also exhibits a strong change. Thus, the plasma potential can again be estimated from the inflection point of the *IV* curve in this region. The plasma potential can also sometimes be estimated using an RPA. Since there is usually always a background population of low-energy ions formed due to charge-exchange collisions or local ionization, these ions will get accelerated across the sheath in front of the RPA and appear as a second low-energy peak in the *IV* curve with an average energy given by the difference between the local plasma potential and the RPA housing potential [60–62]. Comparisons between the plasma potential obtained from emissive probes and RPAs generally show very good agreement [58].

5. Common applications of ion sources

We overview in this section common examples of low-temperature, partially magnetized ion sources. We categorize these broadly into two groups: sources employed for space propulsion and sources employed for material processing. We discuss in each case the principle of operation, application, and common performance metrics.

5.1. Plasma propulsion

Low-temperature plasma sources are widely employed for in-space propulsion applications [63]. The ability of these devices to generate a high energy, collimated ion beam translates to specific impulses an order of magnitude higher than conventional chemical rockets ($I_{sp} > 2000$ s). As a direct result, plasma thrusters have a factor of 5–10 higher propellant efficiency. This advantage is tempered by the fact that due to limited input power on orbit, the thrust of most plasma thrusters is orders of magnitude lower than chemical rockets ($T < 500$ mN). The resulting acceleration on the spacecraft from these thrusters is thus gradual, and the propulsion systems must be operated continuously for days and in some cases years to accomplish maneuvers.

Given these advantages and limitations, there is a premium in plasma thruster design placed on tailoring the ion energy (and therefore specific impulse, I_{sp}) to match the application; increasing the overall efficiency, η (conversion of power to thrust); and in some cases, increasing thrust density, T/A_i. This latter requirement allows for more thrust generation for a given footprint of the thruster, thus incurring lower area and mass penalties. Relating these requirements to the discussion from the previous section, we see that key goals for plasma propulsion sources include lowering ion production cost, increasing the current density, and optimizing the beam energy and quality. In addition, given the long operating times required from these devices, thruster erosion processes and lifetime are also critical factors.

With this in mind, we review in the following sections common types of plasma propulsion, discussing their principles of operation, performance metrics, and applications. We note here that we confine our analysis to plasma systems, i.e. those that rely on the ionization of neutral gas and the subsequent acceleration of charged particles. Our discussion thus excludes other common types of electric propulsion devices such electrothermal arcjets and resistojets and electrospray thrusters.

5.1.1. Gridded ion thrusters. Figure 21 shows a schematic and image of a gridded ion thruster. This device is comprised of an upstream plasma generator and a downstream series of grids for ion acceleration. In the upstream source, a magnetic field is established—typically through a collection of solenoids or concentric ring magnets—to confine the

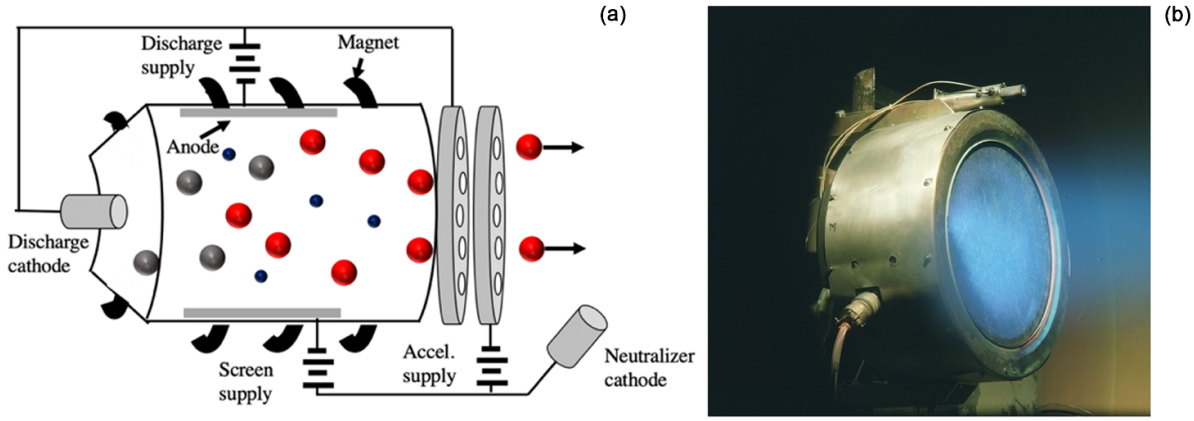

Figure 21. (a) Schematic of a gridded ion thruster with neutrals (gray), electrons (blue), and ions (red). (b) Image of the NASA Solar Technology Applications Readiness ion engine. Image Credit: NASA (Reproduced from www.nasa.gov/feature/glenn/2019/deep-space-1-validates-the-promise-of-ion-thrusters).

Table 1. Common performance metrics for gridded ion thrusters.

η_m	>95%
ϵ_b	100–200 eV/ion
E_i	1000–3000 V
$\langle\sigma_e\rangle / E_i$	<1%
j_i	∼5–10 mA cm^{-2}
η_{acc}	>95%

discharge, and either a DC source (as shown in the figure) or an RF source (usually in the form of an inductive antenna or injected microwaves) is employed to ionize inlet gas. Ions are selectively drawn through the first grid by a small potential drop from the ion source. This also serves to screen incident electrons from entering the grids. A potential bias is then applied between the two grids, accelerating ions to high speed. To maintain spacecraft neutrality, a second 'neutralizing cathode' is employed to inject electrons into the accelerated ion beam.

Table 1 shows typical performance metrics for gridded ion thrusters. As outlined in section 3.3, these devices have relatively low beam divergence, and they can achieve high ion energies ($E_i > 1000$ eV) with low variance. This translates to high specific impulse ($I_{\text{sp}} > 3000$ s) for the typical working gas, xenon. The systems also have among the lowest ion production costs of state-of-the-art ion sources with values on the order of $\epsilon_b = 100$ eV ion^{-1}. Typical operating powers for flight qualified systems range from 0.1 to 7 kW [2].

Gridded ion thrusters suffer from the limitation of space charge density, which places an upper bound on the thrust levels that can be generated for a given cross-sectional area. Scaling them in size thus can be prohibitive for high thrust and power applications. This limitation in turn has driven gridded ion thrusters to designs where the grid spacing is small (<1–3 mm) to maximize current density (equation (8)). The major sources of erosion for these devices historically include the impingement of charge-exchange ions on the downstream grid as well as erosion of the cathodes of hollow cathode. Some devices have demonstrated lifetimes in test exceeding 48 000 h [64].

Gridded ion thrusters have been employed for operational use since the 1960s [65]. Recent applications include station-keeping for commercial spacecraft [63] as well as the main propulsion engine for deep space missions [64, 66–68]. Lower power concepts are also being explored for use on small satellites [69, 70].

5.1.2. Hall effect thrusters. The Hall effect thruster is a type of crossed field device that combines both acceleration and ionization zones. These thrusters (figure 22) are cylindrical with an axial symmetry. A magnetic field is generated across an annular discharge channel while an electric field is applied from an upstream anode to a downstream electron source, typically a type of hollow cathode. Electrons sourced from the cathode are trapped into an $E \times B$ drift—the so-called Hall current—in the azimuthal direction. A neutral gas, which is flowed downstream from the anode, is impact ionized by the trapped electrons. This results in a quasi-neutral plasma state. As the ions are unmagnetized in these devices, they follow the applied electric field and are accelerated out of the geometry to high speed. Additional electrons sourced from the cathode are injected into the accelerated beam to maintain overall thruster neutrality.

Table 2 shows common performance metrics for Hall effect thrusters. These devices typically operate on noble gases, such as xenon and krypton. The ion energies achieved depend on the discharge voltage but typically range from $E_i = 200$–800 V. For xenon, this range corresponds approximately to specific impulses between $I_{\text{sp}} =$ 1500–3500 s. The mass utilization efficiency can be tailored to exceed $\eta_m = 95\%$ for modern devices, and if the magnetic field strength is sufficiently high, the trapped electron current promotes relatively low ion production costs. Due to the quasi-neutral nature of the acceleration process in Hall thrusters, the achievable current densities are an order of magnitude higher than those of gridded ion thrusters. Nominal values are typically $j_i =$100–200 mA cm^{-2} (inferred from [2, 22]). Hall thrusters thus can achieve more thrust for a smaller footprint. This is a major advantage for these systems for flight applications.

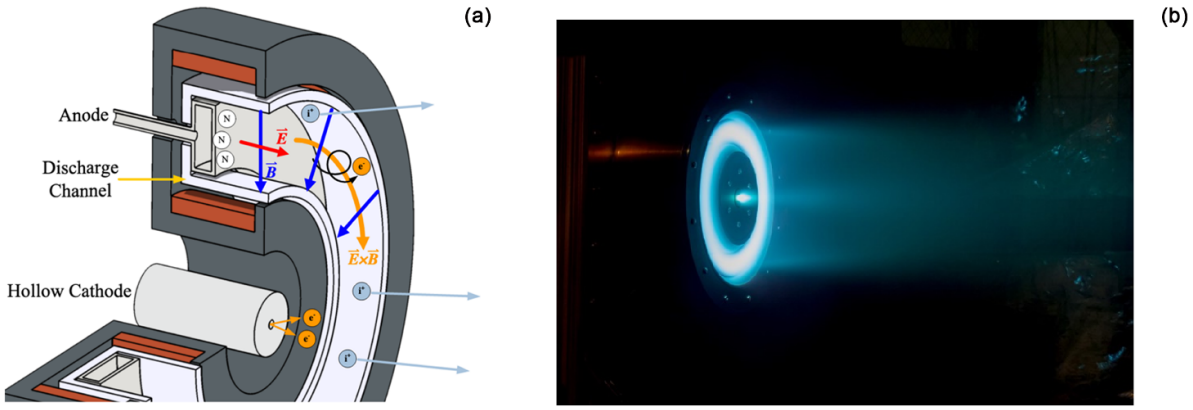

Figure 22. (a) Schematic of Hall effect thruster principle of operation. Reproduced with permission from [71]. (b) 9 kW Hall effect thruster in operation.

Table 2. Common performance metrics for Hall effect thrusters.

η_m	>90%
ϵ_b	150–300 eV/ion
E_i	200–1000 V
$\langle\sigma_e\rangle / E_i$	<10%–20%
j_i	∼100–200 mA cm^{-2}
η_{acc}	>90%

In terms of limitations, since Hall thrusters combine both ionization and acceleration regions, there is a greater dispersion in the energy of accelerated ions. This leads to a larger variance in the energy and loss in acceleration efficiency. Similarly, the need to supply electrons to the discharge incurs a voltage penalty, the so-called cathode coupling voltage [72], that also reduces the acceleration efficiency. The dominant source of erosion and therefore life limiting mechanism of Hall thrusters traditionally has been ion bombardment on the thruster channel walls. While recent innovations in thruster design largely have eliminated this erosion [73, 74], there are more gradual sources of wear that persist on some of the thruster surfaces. Lifetimes are now projected to exceed 50 000 h [75].

Hall thrusters with operating powers ranging from 500 W–12 kW are among the most widely flown type of electric propulsion to date with applications ranging from station keeping and orbit raising to deep space exploration.

5.1.3. Partially-magnetized magnetic nozzles. Figure 23 shows a diagram of the principle of operation of the magnetic nozzle thruster. In this system, which is a type of ambipolar accelerator, a strong diverging magnetic field is applied by either concentric electromagnets or permanent magnets. Gas is then flowed from an upstream manifold, and RF heating is employed to heat the electrons and ionize the gas. Common examples of heating schemes that have been investigated include inductive and helicon-based RF [8, 76, 77] and ECR [9, 10, 78]. Once heated, the electrons then expand along the confining magnetic field, giving rise to the ambipolar field that accelerates the heavier ion species.

A major advantage of the magnetic nozzle is that the strong magnetic field helps reduce wall losses and mitigates plasma interactions with the walls. The former feature enables more efficient operation at smaller scales. It is for this reason that this class of propulsion is under active investigation for small satellite applications where mass and power are limited [69]. The agnosticism to propellant, which is enabled by the lack of plasma wetted electrodes, is a key feature that in principle enables operation on non-traditional gases such as air-based derivatives or condensable propellants like metal and iodine. This is particularly attractive for small satellites applications where the high-pressure storage requirements associated with more traditional propellant gases like xenon and argon represent a possible risk to the spacecraft.

Table 3 shows typical performance metrics for partially magnetized magnetic nozzles. These devices have demonstrated accelerated ion energies as high as E_i =150–200 eV on xenon gas, translating to specific impulses in excess of $I_{\text{sp}} = 1000$ s [9, 18]. The variance of the beam energy is relatively high ($\langle\sigma_e\rangle / E_i > 10\%$), however, due in part to the fact that the heating and ionization schemes are collocated in the system. This leads to more dispersion in the ion beam. The current density of these systems also is moderate to high, $j_i > 25$ mA cm^{-2}. This is enabled by the quasi-neutral nature of the acceleration.

The mass utilization and acceleration efficiency of state-of-the-art magnetic nozzles are both relatively low. This is believed to stem largely from imperfect confinement of the plasma, which curtails the ability to ionize or convert thermal energy into directed kinetic energy through expansion [80]. Indeed, the overall electrical efficiency for low power magnetic nozzles (<100 W) is generally less than 20% [18], though efficiency has been observed to improve with thruster size and power [77]. Partially magnetized nozzle thrusters recently have been flown through a series of technical demonstration missions.

5.1.4. MPD thrusters. Figure 24 shows the principle of operation for a MPD thruster. These axisymmetric devices operate on the principle of Lorentz force acceleration. In a canonical

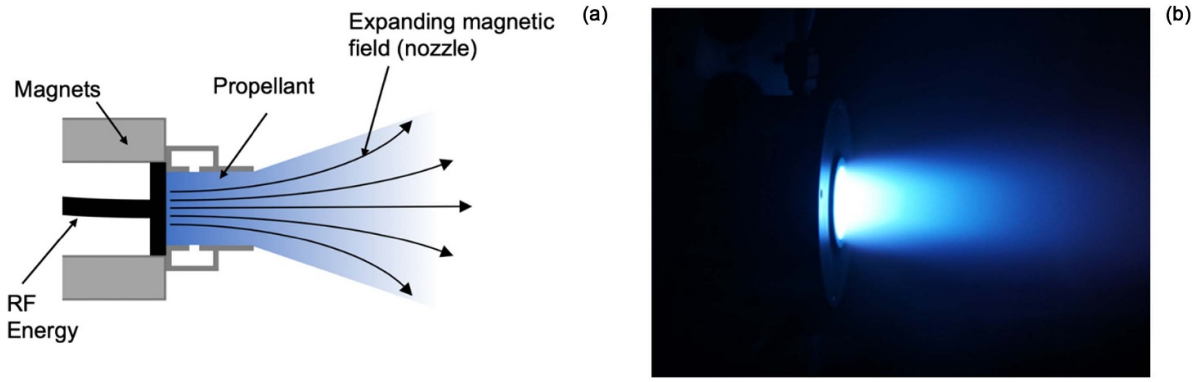

Figure 23. (a) Illustration of principle of operation for a low temperature, partially magnetized magnetic nozzle. (b) Image of an ECR magnetic nozzle thruster operating on xenon at 20 W.

Table 3. Common performance metrics for partially-magnetized magnetic nozzles.

η_m	>40%
E_i	50–200 V
$\langle\sigma_e\rangle / E_i$	>25%
j_i	~25 mA cm^{-2}
η_{acc}	>20%

self-field design, an axially-mounted cathode supports an axial current that drives an azimuthal magnetic field. This current then traverses a radial gap between the cathode and a concentric anode. Gas flowed from the upstream region is impact ionized by this current, and the resulting Lorentz force from the radial current interacting with an azimuthal magnetic field drives axial acceleration of the plasma.

MPDs have been demonstrated over a wide range of operating conditions and configurations, which makes it a challenge to collapse their performance metrics into typyical ranges. In lieu of reporting a table of performance metrics, we thus instead comment on general trends. In particular, we note that MPD thrusters have been operated on a wide range of gases including lithium, xenon, argon, hydrogen, nitrogen, and ammonia [79, 81]. These systems can generate ion energies that exceed $E_i = 300$ eV with high degrees of mass utilization and acceleration efficiency. And as discussed in the preceding section, since MPD thrusters employ Lorentz acceleration, they can achieve higher current and thrust densities compared to other EP concepts. It is largely for this reason that these devices are considered particularly attractive for operation at high powers (>100 kW) [82].

The efficiency of self-field MPDs, i.e. those that rely exclusively on the induced magnetic field interacting with the current, is comparatively low for lower power (<1 MW) operation [81]. As a result, MPDs are often operated with applied fields in the form of concentrically mounted solenoids that can boost the Lorentz force acceleration at lower powers. Historically, the dominant life-limiting mechanism on MPDs has been erosion of the electron source, the cathode, as well as of the surrounding anode. There has been limited technology demonstrations of MPD thrusters in flight to date, most recently through the 1996 Japanese Space Flyer Unit [83] mission. In light of a growing push for higher power concepts as well as recent innovations in superconducting magnets for applied field thrusters, there has been renewed interest in this technology [84–86]. A recent result reported efficiencies approaching 70% at 100 kW of operation [85].

5.1.5. Pulsed inductive thrusters. Figure 25 shows a schematic of a pulsed inductive thruster. In this geometry, a coil embedded in an upstream electrode is pulsed with current, leading to high amplitude azimuthal current in the coil plane. This is provided by, for example, a switch that is closed across a capacitor bank. The current in turn induces a radial magnetic field and a mirror current in the plasma. These latter two interact to drive the ionization and acceleration of the gas. The seed gas for this system is provided by a downstream nozzle that injects along the upstream electrode.

There are many types and geometries for pulsed inductive thrusters including planar, linear, and coaxial accelerators. They all share the common feature, however, that they rely on the mechanism of transiently induced currents to accelerate the propellant. Polzin *et al* [23] has a comprehensive review of these technologies. As with MPDs, the wide range of reported performance metrics for pulsed inductive concepts makes it difficult to assign typical ranges to these devices. We therefore forgo including a table in this section as well.

Pulsed inductive thrusters are an attractive technology for propulsion applications for two primary reasons. The first is that, as with magnetic nozzles, they minimize interaction between the propellant and accelerating electrodes. They thus can operate on more reactive non-traditional propellants like air and water. The second advantage stems from their throttleability. In principle, the physics of acceleration and ionization are confined to the duration of the pulse inducing the current. Thus, by varying the duty cycle of the pulses, the power and thrust can be throttled while maintaining overall efficiency and average energy of the system.

While some pulsed plasma thrusters have been flown to date, these systems are not at the same level of maturity or in widespread use as Hall or gridded ion thrusters. Major challenges with their implementation include the need for long life

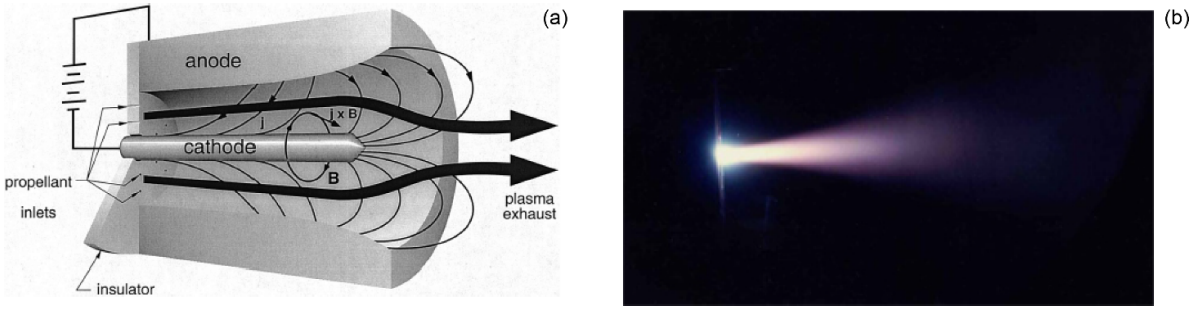

Figure 24. (a) Illustration of principle of operation for a MPD thruster. From [79]. Reprinted by permission of the American Institute of Aeronautics and Astronautics, Inc. (b) Image of an MPD thruster firing. Image Credit: NASA (Reproduced from www.nasa.gov/centers/glenn/about/fs22grc.html).

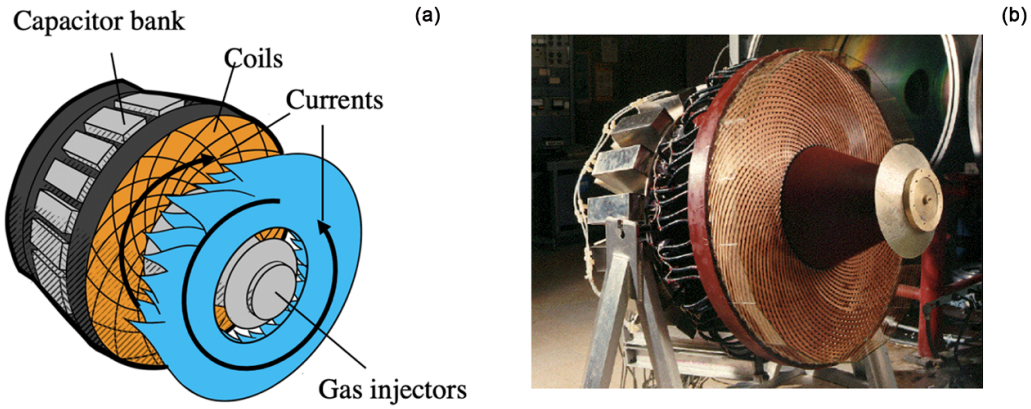

Figure 25. (a) Illustration of principle of operation of planar pulsed inductive thruster. Reproduced with permission from T Gill, University of Michigan. (b) A pulsed inductive thruster with spiral coil Image Credit: NASA (Reproduced from www.nasa.gov/centers/glenn/about/fs22grc.html).

switches and gas delivery systems capable of pulsing for millions of cycles [23].

5.2. Materials processing: applications

Plasma processing typically refers to the use of plasmas to modify or create different materials to enhance or achieve specific desired material properties or shapes. Plasmas can be used for both subtractive manufacturing (e.g. etching and milling), as well as additive manufacturing (deposition). In the semiconductor industry for example, these techniques are often used at different stages during the manufacturing process of important functional devices such as transistors and integrated chips (ICs) [3, 6].

In comparison with purely mechanical or equilibrium chemical processing methods, plasmas enable very precise material processing and the formation of structures with nano and micrometre scale features. As low-pressure plasmas are non-equilibrium, they can be used to produce surface layers, crystal morphologies, or device structures with improved properties or chemical compositions that are unobtainable with pure chemical methods at any temperature [3]. They also allow processing at much lower material temperatures, which eliminates undesired chemical or material changes (such as melting) and reduces thermal distortion.

Materials processing is an interdisciplinary field that involves plasma physics, chemistry, atomic and molecular physics, and surface science. Given the complex coupling between these different areas, and the wide range of applications in very diverse fields, the literature on materials processing is vast. In this section, we therefore only briefly describe the main processing methods while highlighting some commonly used plasma sources and their role.

5.2.1. Plasma etching. Modern semiconductor devices, such as ICs, consist of many layers of specially engineered thin films arranged in sophisticated configurations. These thin layers are produced using deposition processes and are etched using reactive plasmas to form specific patterns with small-scale features typically of the order of tens of nanometres. Etching is a process that involves reactive gas-phase species interacting with a solid surface to produce a volatile gaseous product. By using patterned masks, preferential etching can occur to obtain particular patterns and shapes on a target surface. For the etching of silicon-based materials, different halogen-containing molecules, such as SF_6, are used and can achieve different etching properties. These reactive gases are introduced into a plasma, and electron-neutral impact collisions leads to dissociation and the formation of different reactive species such as fluorine atoms.

Similar to wet chemical etching (i.e. pure chemical etching without a plasma), etching with neutrals occurs isotropically. In general, this is unsuitable for the manufacture of many devices which instead require high aspect ratio (i.e. width-to-depth ratio) etch features [3, 87]. However, bombarding a surface with energetic ions in addition to neutral chemical etchant species can lead to a total etching rate that is larger than that due to the ion or neutral species separately by themselves (often by a factor of 5–10) [88, 89]. The reasons for this enhanced etching are still not completely understood but are thought to be chemical in nature and related to ion-enhanced chemical reactions or ion-enhanced desorption of chemical etch products [3]. Because of the plasma sheath in front of the substrate, ions are electrostatically accelerated through the sheath with trajectories that are perpendicular to the surface. This use of ions helps to promote anisotropic etching while minimizing side-wall etching is known as reactive ion etching (RIE) [90]. The high reactivity gases used during RIE allows high material selectivity of the etch, adjustable etch feature profiles, and high etch rates [87].

Although RIE improves etch anisotropy, this may still not be sufficient for some applications. In this case, further processing gases are introduced that promote the formation of polymerizing coatings which are etch resistant or inhibiting [91, 92]. These coatings, or passivation layers, form on the walls of the etch feature, but because of continual ion bombardment from the plasma, are disrupted on the plasma-facing bottom surface. This establishes a preferential direction for etching, allowing higher aspect ratio features, and again highlights the critical role played by energetic ions.

Etching is an important process used in the manufacture of semiconductor devices such as metal-oxide-semiconductor field effect transistors (MOSFETs) used in large-scale ICs [3]. It is also used in photonics and optoelectronics to create high aspect ratio features [92, 93] and in the fabrication of micro-electro-mechanical systems (MEMS) components [93, 94]. Plasmas and ion sources are typically based on RF discharges such as CCPs, ICPs, and helicon or microwave plasmas [90].

Etching within the semiconductor industry is an important field that is discussed in more detail in the companion Foundations paper in [95].

5.2.2. Plasma deposition. Deposition is an additive manufacturing process that allows the creation of thin films with different properties and thicknesses. In contrast to chemical vapour deposition (CVD), plasma-enhanced CVD (PECVD) enables films to be deposited at much lower temperatures and with improved properties [17]. Often, parameter spaces can be reached which are not possible using equilibrium chemical methods, thus allowing thin films with unique chemical compositions or crystal structures to be obtained that are not otherwise found in nature [1, 2].

By creating a plasma using a mixture of feedstock gases (including reactive gases), different species can be formed through electron-impact dissociation and chemical reactions between reactive gas-phase precursors [3]. The chemistry is chosen so that desired reaction products condense or deposit onto the substrate surface [96]. In PECVD the gas phase and surface reactions are controlled and strongly modified by the plasma properties. To facilitate chemical reactions between neutral gas species, higher pressures are used than those in etching processes, and CCPs are often favoured due to their ability to produce uniform plasmas over large area. By varying the plasma and ion bombarding properties at the substrate, the film composition, mechanical stress, and film integrity can be controlled to increase reliability and performance [97].

PECVD is an important process for the deposition of thin films in semiconductor devices and the fabrication of flat-panel displays such as TV or computer screens [98]. Such displays make use of thin film transistors that are manufactured using a series of thin film deposition steps [6]. PECVD can also be used in the growth of films for optical [96] and photonic [99] applications, the manufacture of solar cells [100], and growing carbon nanotubes [101].

CVD and PECVD is discussed in more detail in the companion Foundations papers in [102, 103].

Thin films can also be created using a physical deposition process that does not rely on chemistry. When high-energy ions strike a target surface they lead to the physical removal of surface atoms in a process known as sputtering [3]. The number of atoms removed, known as the sputter yield, is a strong function of the ion energy, incidence angle, target material, and bombarding ion. The ejected atoms are then sprayed onto a substrate surface placed in close proximity to the target and thin films build up over time [104]. Sputtering is a useful technique for depositing metal films as it is a non-thermal physical process that does not rely on chemical reactions and can even be used to deposit refractory metals. Generally, good film uniformity, surface smoothness, and surface adhesion can be obtained over large areas.

Sputtering can be achieved using both local and remote ion sources. For example, remote broad beam gridded ion sources can produce high-energy ions using reactive or non-reactive gases [104, 105]. Alternatively, a background plasma can be produced and the target negatively biased so that background ions are accelerated by the electric fields in the target sheath itself. DC magnetrons are commonly used as sputtering sources [106].

By adding multiple ion sources with different target materials, films of metal alloys can be deposited on the substrate. Multiple ion sources can also be used to provide extra ion bombardment of the substrate itself to influence film growth or to pre-clean the substrate before sputter deposition begins. Using reactive gases, such as oxygen, allows dielectrics to be deposited in a process known as reactive sputtering [105, 107]. Here a plasma dissociates the feedstock gas, and the reaction products chemically interact with the target. Deposited films are then a compound of the sputtered target material and the reactive gas. This process is typically used for deposition of oxide or nitride films.

Sputtering has many different applications [106] including the deposition of metal films for electrodes and interconnection layers in ICs, optical coatings, and corrosion

resistant films for decorative purposes. In propulsion applications, sputtering is an undesirable phenomenon that leads to erosion of critical components (such as ion acceleration grids) and subsequent performance drifts or eventual system failure [2]. Propulsion systems need to be carefully designed to minimize or eliminate sputter erosion.

5.2.3. Ion implantation. In contrast to deposition where thin films are deposited above a substrate surface, ion implantation is used to modify layers below the substrate surface [108]. Ion implantation is a fundamental process in semiconductor manufacturing and is used to dope silicon with certain elements to obtain different desired properties [109]. Silicon is neither a pure conductor nor a pure insulator, but by inserting specific elements into the silicon crystal lattice, control of the current flow can be obtained. For example, doping silicon with p-type dopants, such as boron, creates an excess of positive charge carriers, while n-type dopants, such as phosphorous, creates an excess of negative electron charge carriers. The combination of p-type and n-type silicon structures forms the basis of many semiconductor devices [3, 6].

Silicon doping requires specific elements to be embedded within the substrate material and this can be achieved by implantation. Here a plasma is created in a chamber and ions are extracted and accelerated to very high energies (typically of the order of 10's to 100's of keV) [109]. Ions penetrate the substrate and replace silicon atoms in the crystal structure. The ion energy establishes the effective penetration depth, while the ion current defines the number of atoms being implanted. With this substitution of silicon atoms, the near-surface region of the substrate is modified.

Plasma-immersion ion implantation (PIIM) is a technique to implant ions which removes the need for a remote ion source, and consequently the extraction/focusing electrodes and any beam scanning subsystem [110]. Here, the target is physically immersed into a plasma environment and implantation is achieved by applying a series of very high-voltage negative pulses to the target which then accelerate plasma ions. This is a particularly attractive technique for processing non-planar targets.

Ion implantation has been used for biomedical applications [111, 112], doping of silicon trenches, the fabrication of special MOSFETs, and surface modification to improve wear, hardness, and corrosion resistance [113].

5.2.4. Precision machining. While sputter erosion can be used to deposit thin films, it is also an effective mechanism that can be exploited to achieve high precision machining using broad-beam [114] or focused ion beam (FIB) sources [115]. For example, FIBs are used for direct milling to locally remove material in the creation MEMs and nano-electro-mechanical systems devices and have been used to fabricate miniature Fresnel lens and nano-fluidic devices in silicon.

Typically, a plasma or liquid metal source is used to extract ions which are then accelerated using electrostatic lenses or grids [105]. The size and depth of milled features are effectively controlled by the dwell time of the ion beam which can also be scanned over the target. Precision machining with feature resolutions as low as a few nanometres are possible. Milling is a physical sputtering process, so wet chemical processing, patterning masks, or photoresist materials are not required. By adjusting the ion beam energy, current, and incidence angle, the material removal rate can be finely controlled, allowing complex shapes and patterns to be produced. In addition, the ability to use inert gases such as argon eliminates undesired chemical or corrosion processes.

Ion sources for precision machining have been used for tomography and reverse engineering [116], sample preparation [117], creating complex 3D microstructures [118], and smoothing or polishing of surfaces such as x-ray mirrors to reduce microroughness [119].

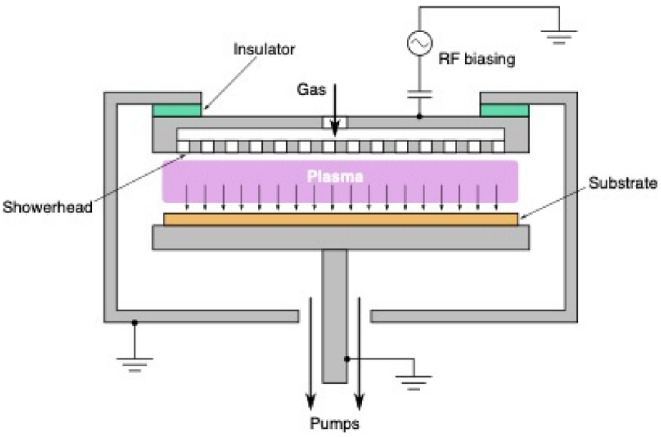

Figure 26. Schematic of a single-frequency CCP.

5.3. Materials processing: sources

5.3.1. Capacitively coupled plasmas. CCPs typically consist of two parallel-plate electrodes separated by a gap of the order of 1–10 cm [3, 6]. An RF voltage is applied to one of the electrodes while the opposite electrode is grounded. Since the radial walls of the reactor are also usually grounded, the CCP discharge is typically asymmetric. Feedstock gases are injected through a showerhead design, and for a sufficiently high RF voltage, a plasma discharge can be ignited and sustained between the electrodes. CCPs are an example of a local plasma source since the plasma is formed in the vicinity of the material to be processed which is located on, or integrated with, one of the electrodes. Figure 26 shows a schematic of a typical single-frequency CCP.

CCPs can be operated over a wide range of conditions depending on the specific application [3, 6, 90]. For etching, the ion bombarding energy and angular distribution is important and the discharge may be operated at lower pressures, while for deposition, higher pressures may be necessary to reduce the ion energy to prevent thin film damage. Plasma densities in CCPs are typically between 10^{15}–10^{17} m^{-3} with an electron temperature around 3 eV. Device sizes can range from small table-top reactors for R&D [120] to large

room-sized reactors such as those used in the manufacture of flat-panel displays [98]. Applied RF frequencies can be as low as 2 MHz or as high as 90 MHz.

CCPs are favored for many applications because they can achieve good plasma uniformity over large areas, and can be operated even with insulating electrodes [3, 6]. However, CCPs generally exhibit a low power coupling efficiency with the plasma, even when using an impedance matching network, and produce lower plasma densities because of the higher plasma kinetic energy losses at the electrodes due to the applied RF voltage. It is also not possible to separately control the ion flux and ion energy in a single-frequency discharge [121].

Unlike with the ion sources for space propulsion discussed in section 5.1, some of the figures of merit introduced in section 2.2, such as the propellant utilization, are of little or no direct interest (due to the required operating pressures and device functional requirements). Of more relevant interest is the ion flux, energy, and angular distribution, which play important roles in the material surface physics and in determining the processing rate. The ion flux is typically in the range 10^{18}–10^{20} m^{-2} s^{-1}, which gives current densities between about 0.02–2 mA cm^{-2}, while the average ion energy can go from less than 100 eV to above 1000 eV depending on the specific application. The variance around the average ion energy can also vary widely, going from $\sigma_E/E_i \sim 1\%$–5% at very low pressures and high RF excitation frequencies to above 50% at high pressures and low frequencies.

5.3.2. Inductively coupled plasmas. Compared with CCPs, higher plasma densities and fluxes (and hence processing rates) can be obtained by instead using an ICP [6, 122, 123], a schematic of which is shown in figure 27. Here, an RF antenna is located external to the plasma itself and is either wrapped around an insulating tube in cylindrical geometries, or is a flat spiral coil separated from the plasma by an insulating window in planar geometries [3]. The material to be processed is then located on a substrate that is placed downstream of the RF antenna. The time-varying electromagnetic fields generated by this antenna couple inductively to the plasma, and power is transferred without any immersed electrodes [6]. This results in a significantly lower potential drop across the wall sheaths that reduces plasma kinetic energy losses and allows higher plasma densities to be obtained. For applications requiring higher ion energies, the substrate onto which the material is placed can be RF biased allowing separate control of the ion energy [90]. Power coupling efficiency between the antenna and the plasma is also usually enhanced in ICPs and can reach values as high as 90% [6, 123].

Plasma densities are typically between 10^{17}–10^{19} m^{-3} with operating pressures of the order of 0.1–1 Pa, and RF frequencies equal to 13.56 MHz or 27.12 MHz [3, 6, 90, 122, 123]. The main disadvantage of ICPs is that they generally produce non-uniform radial profiles which can lead to different processing rates on the center and edges of the substrate.

Although ICPs are widely-used, alternative plasma generation and heating methods have also been implemented.

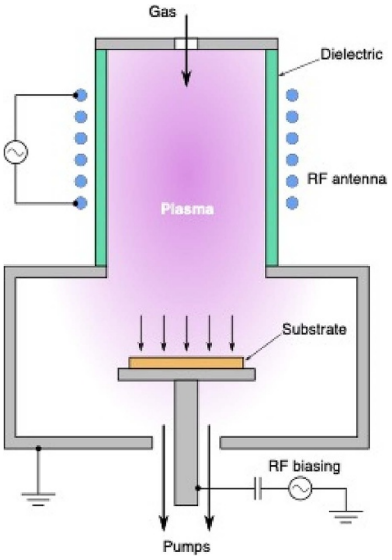

Figure 27. Schematic of an ICP.

These include wave-heated discharges such as Helicon and microwave ECR discharges [3, 124]. Here, an external magnetic field is now applied and is important in accessing specific operating modes. For example, the magnetic field influences the plasma permittivity allowing the propagation of electromagnetic waves from an RF antenna as in Helicon discharges [3, 7]. This can improve power coupling efficiency under some operating conditions and can lead to remote electron power absorption away from the RF antenna itself. The shape of the applied magnetic field also plays an important role in plasma transport and controlling plasma uniformity above the substrate [124], and usually diverges downstream of the RF antenna (somewhat similar to the magnetic nozzles used in ambipolar thrusters). In ECR discharges, the magnetic field causes electrons to precess and at certain locations within the discharge this precession is resonant with the rotation frequency of the right-hand polarized wave component of injected microwaves [3] leading to power absorption. Typical Helicon and microwave frequencies are 13.56 MHz and 2.45 GHz respectively.

ICP and ECR discharges are also commonly used for plasma generation in gridded ion thrusters [125, 126]. Since these discharges are electrodeless, the operating lifetime of the plasma source can be higher than equivalent DC ion thrusters, and more reactive gases such as iodine [125] can be used.

5.3.3. Gridded ion sources. These sources share many similarities to gridded ion thrusters and are often used for sputtering, etching, deposition, and precision machining [123, 127, 128]. An image of an example source is shown in figure 28. A low-pressure plasma is generated in a chamber using either a DC discharge, an ICP, or ECR [128], and ions are extracted and accelerated by a set of grids. The target material to be processed is then located downstream of the grids. An

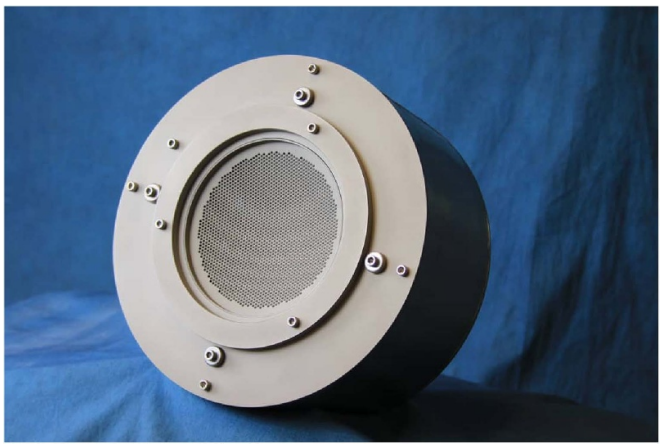

Figure 28. Image of an RF gridded ion source. Image Credit: Plasma Process Group. Copyright 2022 Plasma Process Group, Inc. All rights reserved.

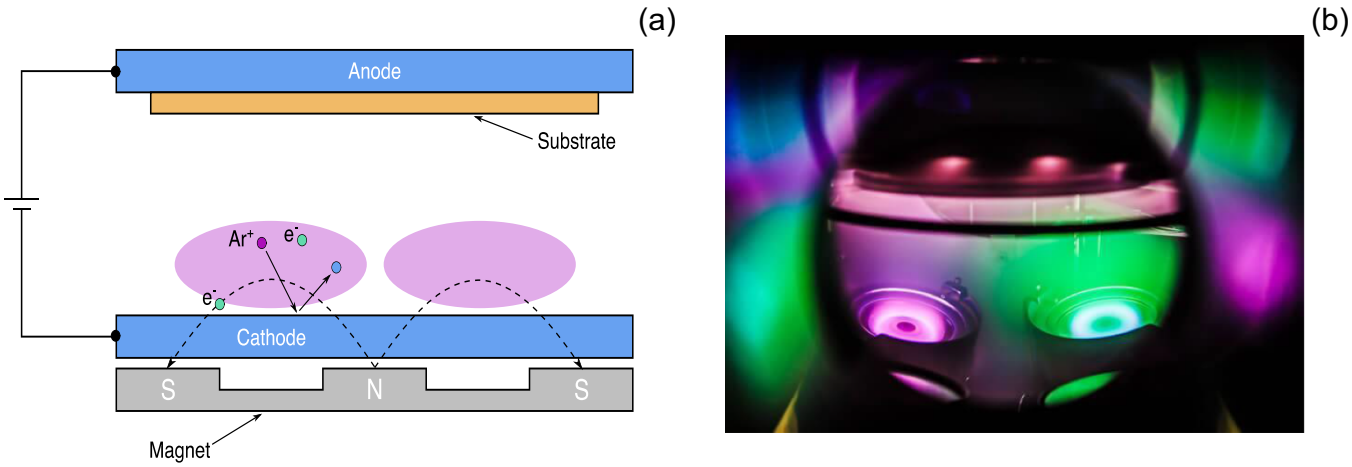

Figure 29. (a) Schematic of a magnetron. (b) Image of a pair of magnetrons in operation. Image Credit: Angstrom Engineering Inc. Copyright © 2022 Engineering Inc.

electron-emitting neutralizer may be used to prevent material charging.

The design of gridded sources for materials processing requires a careful balance between extracted ion beam current (which influences the processing rate) and the size and geometry of the grids/ion optics [105, 128, 129]. For example, FIBs may use high voltages and small electrodes with good focusing to produce an intense ion beam, while for etching the ion optics may be larger to maximize uniformity. Whereas ion beam divergence is usually minimized for space propulsion applications, a higher beam divergence may be desired for some applications such as deposition.

Because of its inert nature, physical properties, and cost, argon is a commonly used gas in gridded ion sources. Extracted ion beam currents can be as high as 100–1000 mA with ion energies between 100–1000 eV [127]. Gridded ion sources are usually operated at low pressures to minimize ion-neutral collisions that can lead to grid erosion and energy-spreading of the ions. Source design involves optimization to reduce the ion production cost and increase feedstock gas utilization efficiency. So long as ions are focused through the grid apertures and the space-charge limit is not reached, separate control over the ion energy and ion flux can be obtained by adjusting the grid acceleration voltage and the plasma source power.

5.3.4. Magnetrons. These devices consist of a planar disk-shaped cathode connected to an anode typically several centimeters away onto which a substrate is placed (see figure 29). An axisymmetric, annular, permanent magnet is located below the cathode, not in direct contact with the plasma, and a plasma discharge is produced typically in a background argon gas by applying a voltage across the anode and cathode [3, 130]. Argon ions are then accelerated through the cathode sheath and sputter the cathode which is made of a metal of interest to be deposited onto the substrate. The bombarding ions also lead to secondary electron emission from the cathode which is responsible for maintaining the discharge. The presence of the magnetic field helps to increase the confinement of these

secondary electrons to improve discharge efficiency and allow operation at lower pressures [130].

Operating pressures are usually of the order of 1 Pa or lower, with an applied voltage of around 1000 V or less, and a magnetic field strength typically of the order of 100 G [130]. Because of the magnetic field, the plasma discharge is often a bright circular ring with most of the sputtering occurring from a corresponding ring-shaped track on the cathode under the plasma [130] as illustrated in figure 29. This bright high-density quasi-neutral plasma shields out electric fields and most of the applied discharge voltage is dropped across a narrow sheath region, typically of the order of 1 mm, in front of the cathode. The aspect ratio of the cathode-anode gap to discharge radius is an important factor in controlling the uniformity of deposited thin films. Magnetrons are widely used to sputter metal cathode targets to produce thin films through deposition on the substrate. For sputtering of insulators such as ceramics, an RF voltage is applied across the electrodes [130].

Magnetrons can also be operated in a high-power pulsed mode, such as in high power impulse magnetron sputtering (HIPIMS) [131]. Here, the cathode current density can be increased by 1–2 orders of magnitude with corresponding higher plasma and power densities. A significant fraction of the sputtered target material is also ionized [132]. HIPIMS can lead to enhanced film properties that can be more precisely controlled by adjusting the characteristics of the applied pulses [133].

6. Future outlook for technology

Now that we have established the principles of operation, common diagnostics, and key applications for low temperature ion sources, we turn in this section to a discussion of the future outlook for this technology. In particular, we highlight the need for both development and fundamental research.

6.1. Trends in propulsion

Plasma propulsion has been widely adopted for in-space applications, and given its high propellant efficiency, this technology will continue to remain a staple for the space industry [63]. With that said, there are several technical challenges that remain for the advancement of these systems [134]. These primarily relate to the need to expand the traditional operating envelope to accommodate a growing demand for versatility and resilience in space.

For example, in a recent study released by the National Academy of Science, nuclear-powered plasma propulsion was highlighted as a key technology for enabling crewed missions to Mars [82]. This report identified several outstanding challenges with achieving this future goal, including the need to reduce the specific mass (mass per unit power) of propulsion systems and to extend lifetime. To this end, a key research goal for future efforts will be to explore methods for increasing the effective thrust and power density of propulsion systems. While MPD thrusters are a leading candidate for this purpose, Hall thrusters also have been identified as a promising alternative—provided they can maintain performance and efficiency at the required power levels [135]. Similarly, alternative design strategies for gridded ion thrusters may help overcome space-charge limitations to achieve higher thrust density and lower specific mass [136]. There is also a form of magnetic nozzle with a fully magnetized plasma—the Variable Specific Impulse Magnetoplasma Rocket—that has been investigated as a possible solution for high power density operation [137].

In addition to exploring the high-power limits of electric propulsion systems, there is also a growing need to extend the operating envelope of plasma propulsion to lower power levels (<500 W) to accommodate the rapidly increasing number of small satellites in orbit [69, 70]. Propellant-efficient propulsion for these micro systems is critical for station keeping, drag make up, and in some cases, orbit raising. There are several challenges with scaling this technology to this size, however. Most notably, higher confinement losses lead to overall reductions in efficiency (section 2.2).

Plasma propulsion systems that operate on non-traditional propellants are also opening new possibilities for the field. For example, air-breathing propulsion concepts could in principle support spacecraft that use atmosphere to perform drag make up at extremely low altitudes [138]. Similarly, thrusters capable of '*in situ* resource utilization' by harvesting propellants from space environments, e.g. water or carbon dioxide, enable unique mission architectures for deep space exploration. The ability to operate on condensable propellants like iodine is particularly attractive for small satellite applications where storage of pressurized gases like the more traditional xenon and krypton poses a major risk [125]. There is also a demand for plasma propulsion systems that use the combustion products of so-called energetic propellants. This is motivated by the need for dual mode systems, i.e. the ability use more traditional chemical engines for high thrust, low specific impulse maneuvers and plasma propulsion for low thrust, high specific impulse maneuvers [139].

For alternate propellants to become widespread, several technical challenges will need to be overcome. For example, there is the possibility of an adverse reaction of energetic propellants—particularly ones with oxygen-based products—with the thruster body. More fundamentally, the ionization cross-sections for many of these alternative propellants are lower than those of the traditionally-employed xenon, leading to reduced mass utilization efficiency and performance.

In parallel with the demand for new technologies and propellants, there is also a recognized need for improved testing capabilities for these systems. For example, to approximate on-orbit behavior for plasma propulsion devices, it is necessary to recreate a high-level vacuum environment. It is well established, however, that there are aspects of vacuum test facilities, like the presence of residual gas, that can impact thruster operation. These effects can lead to discrepancies in performance as measured during ground tests versus what would be observed during flight [10, 72, 140–143]. There is thus considerable interest in assessing the role of facilities on key aspects of thruster operation e.g. beam energy, thruster efficiency, and lifetime, and in turn how to map performance on the ground to flight. In conjunction with the need for

improved testing capabilities, lifetime qualification through both direct testing and analysis is also a major challenge for the next generation of plasma propulsion [144].

As a final consideration, we note that in addition to challenges with technology development, there are several outstanding physics-based questions related to ion sources for plasma propulsion. Most pressingly, as identified in the recent 2017 roadmap and 2020 Plasma Science Decadal survey [1, 145], the roles of plasma instabilities and self-organization remain poorly understood in these systems. These processes are of practical importance as they can impact stability, beam quality, and efficiency. The role of instability-driven anomalous cross field electron transport is of particular importance for the study of Hall thrusters and magnetic nozzles where this process can dominate the electron dynamics [146].

6.2. Trends in materials processing

In contrast to space propulsion where the primary objective is typically to produce an ion beam as efficiently as possible for thrust generation, ion sources for materials processing can have widely varying requirements depending on the application. While ion source power efficiency and feedstock gas usage efficiency are always of interest, the primary driving factor is more often fit for purpose processing functionality.

Although certain fundamental device size limits are now being approached, plasma-based technologies are expected to continue playing a vital role in the materials processing industry and still represent the only viable processing method available today in many cases [147]. The shrinking of semiconductor devices, and interest in next-generation *post-silicon materials,* nonetheless presents several significant challenges that require both technical and physics-based advances. Current challenges include improving control over species fluxes and ion energy and angular distributions, as well as improving microscopic and macroscopic processing uniformity [87]. Further challenges and industry needs are summarized in [1, 87] and discussed in companion Foundations papers [95, 102, 103].

Starting at around 1 μm in the 1980s, the dimensions of critical semiconductor devices have shrunk by around two orders of magnitude with dimensions below 5–10 nm of interest today [1, 87]. Atomic-level processing precision is of great interest to achieve thin films and surface features with such small sizes, as well as to reduce absolute dimensional tolerance variability [148, 149]. For deposition, plasma-enhanced atomic layer deposition (PEALD) can increase the type of films that can be deposited because of lower temperatures, the unique reactive species formed, and the presence of energetic ions [150]. However, the large number of species produced using typical feedstock gases can lead to competing surface reactions. In addition, while energetic ions are useful for treating films, their angular distribution tends to be very anisotropic due to acceleration through the sheath in front of the target process material. Thus, these ions do not equally treat the sidewalls and bottom wall of high-aspect ratio features for example [1]. If the ion energy is too high, then damage to films can also occur. Thus, aside from better control of the reactive species generated within the plasma, a significant challenge from an ion source perspective is improved control over the ion energy and ion angular distribution functions.

Similarly, PEALE is of growing interest where material layers can be removed with atomic-level precision [151, 152]. This requires high selectivity of the etch process so that unetched materials remain pristine and undamaged. As with conventional plasma etching, plasmas act as a good source of reactive species and energetic ions that can enhance the directionality of the etch [153]. Challenges in this case relate to microscopic etch uniformity, since the etch rate can depend on feature size (aspect ratio-dependent etch), while ions can remove several atomic layers due to the typical energies encountered in common plasma sources. This can again lead to surface damage. Several interesting plasma source designs have been proposed to address some of the above issues, including the use of neutral beams [154] formed through charge-exchange or surface neutralization of positive or negative ion beams which also eliminate charging, and electron beam-generated plasma sources [155] which produce low bulk plasma electron temperatures and corresponding sheath potentials and ion energies.

Plasma and process uniformity is also an important challenge in manufacturing. For some applications, such as precision machining, the ion source or target material can be mounted onto motorized translational or rotational stages and the machining rate controlled by the dwell time at each position. For other applications, such as plasma deposition and etching, better uniformity inherent to the plasma source itself is needed. For example, most plasma sources exhibit a radial density or beam profile with different fluxes to the center of a process target than the edges. This leads to different processing rates and increased variability in deposited thin film or etch features. RF CCPs offer significant uniformity advantages due to the nature of these discharges which essentially produce a plasma between parallel-plate electrodes, but other problems can emerge. For example, in single-frequency CCPs the ion flux and ion energy cannot be separately controlled [121]. Thus, a higher flux for increased processing rates will produce higher energy ions that could lead to material surface damage. In addition, for large-area CCPs such as those used in the manufacture of flat-panel displays, electromagnetic effects and standing waves can appear at high frequencies [156], causing electrodes to no longer be equipotential. This can further exacerbate radial non-uniformities.

Dual-frequency CCP discharges offer some improvement in process control where the high-frequency component controls the plasma density/flux and the low-frequency component offers ion energy control [157]. However this can still be limited due to frequency coupling [158, 159], particularly in the presence of materials with high secondary electron emission coefficients. Within the last 10 years, a more promising technique involving the use of tailored waveforms has emerged [160] which allows better control over the electron distribution function and hence plasma species produced

[161], separate control over the ion flux and ion energy [162], and even the ion energy spread [163] through the use of custom waveforms composed of several harmonics with different amplitudes and phase shifts. There is also some evidence that such waveforms can lead to improved uniformity [164]. Current challenges relate to effective impedance matching of multiple frequencies, although some solutions have been proposed [165, 166], and the use of operating conditions and feedstock gases of closer interest to industry [167].

As with the previous section on propulsion, there are also several physics-based challenges that remain. These largely relate to improving our understanding of plasma-surface and gas-surface interactions [1], which are central to the functionality and applicability of most materials processed with plasmas. This requires fundamental studies of different surface processes and enhanced modelling based on quantum chemistry and molecular dynamics simulations. Although this may be viewed predominately as a 'material' or 'surface' problem, a better understanding of these processes is important for the design and optimization of plasma and ion sources which are ultimately used to process such materials.

Data availability statement

No new data were created or analysed in this study.

Acknowledgments

The authors would like to acknowledge Thomas Marks, Christopher Sercel, Parker Roberts, and Leanne Su from the University of Michigan for reviewing the manuscript.

ORCID iDs

Benjamin Jorns https://orcid.org/0000-0001-9296-2044
Trevor Lafleur https://orcid.org/0000-0002-9926-2187

References

[1] Adamovich I *et al* 2017 The 2017 plasma roadmap: low temperature plasma science and technology *J. Phys. D: Appl. Phys.* **50** 323001
[2] Goebel D M and Katz I 2008 *Fundamentals of Electric Propulsion: Ion and Hall Thrusters* (*JPL Space Science and Technology Series* vol 1) (New York: Wiley)
[3] Lieberman M A and Lichtenberg A J 2005 *Principles of Plasma Discharges and Materials Processing* (New York: Wiley)
[4] Chen F F 2015 Helicon discharges and sources: a review *Plasma Sources Sci. Technol.* **24** 14001
[5] Geller R 1990 ECRIS: the electron cyclotron resonance ion sources *Annu. Rev. Nucl. Part. Sci.* **40** 15–43
[6] Chabert P and Braithwaite N 2011 *Physics of Radio-Frequency Plasmas* (Cambridge: Cambridge University Press)
[7] Boswell R W and Chen F F 1997 Helicons-the early years *IEEE Trans. Plasma Sci.* **25** 1229–44
[8] Lafleur T, Cannat F, Jarrige J, Elias P Q and Packan D 2015 Electron dynamics and ion acceleration in expanding-plasma thrusters *Plasma Sources Sci. Technol.* **24** 065013
[9] Cannat F, Lafleur T, Jarrige J, Chabert P, Elias P-Q and Packan D 2015 Optimization of a coaxial electron cyclotron resonance plasma thruster with an analytical model *Phys. Plasmas* **22** 053503
[10] Wachs B and Jorns B A 2020 Background pressure effects on ion dynamics in a low-power magnetic nozzle thruster *Plasma Sources Sci. Technol.* **29** 045002
[11] Dannenmayer K and Mazouffre S 2008 Sizing of Hall effect thrusters with input power and thrust level: an empirical approach pp 231–54
[12] Su L L and Jorns B 2021 Performance at high current densities of a magnetically-shielded Hall thruster *Proc. 2021 AIAA Propulsion and Energy 2021 Forum August 2021* AIAA-2021-3405 (https://doi.org/10.2514/6.2021-3405)
[13] Ahedo E and Merino M 2010 Two-dimensional supersonic plasma acceleration in a magnetic nozzle *Phys. Plasmas* **17** 073501
[14] Merino M and Ahedo E 2015 Influence of electron and ion thermodynamics on the magnetic nozzle plasma expansion *IEEE Trans. Plasma Sci.* **43** 244–51
[15] Little J M and Choueiri E Y 2016 Electron cooling in a magnetically expanding plasma *Phys. Rev. Lett.* **117** 1–5
[16] Ahedo E, Correyero S, Navarro J and Merino M 2020 Macroscopic and parametric study of a kinetic plasma expansion in a paraxial magnetic nozzle *Plasma Sources Sci. Technol.* **29** 045017
[17] Martinez-Sanchez M, Navarro-Cavallé J and Ahedo E 2015 Electron cooling and finite potential drop in a magnetized plasma expansion *Phys. Plasmas* **22** 053501
[18] Vialis T, Jarrige J, Aanesland A and Packan D 2018 Direct thrust measurement of an electron cyclotron resonance plasma thruster *J. Propuls. Power* **34** 1323–33
[19] Ahedo E and Merino M 2011 On plasma detachment in propulsive magnetic nozzles *Phys. Plasmas* **18** 053504
[20] Jahn R G 1968 *Physics of Electric Propulsion* (New York: McGraw-Hill)
[21] Coogan W J and Choueiri E Y 2017 A critical review of thrust models for applied-field magnetoplasmadynamic thrusters *53rd AIAA/SAE/ASEE Joint Propulsion Conf. June 2017* pp 1–27
[22] Dannenmayer K and Mazouffre S 2011 Elementary scaling relations for Hall effect thrusters *J. Propuls. Power* **27** 236–45
[23] Polzin K, Martin A, Little J, Promislow C, Jorns B and Woods J 2020 State-of-the-art and advancement paths for inductive pulsed plasma thrusters *Aerospace* **7** 1–67
[24] Turner M M and Chabert P 2014 A radio-frequency sheath model for complex waveforms *Appl. Phys. Lett.* **104** 164102
[25] Chabert P and Turner M M 2017 A model for tailored-waveform radiofrequency sheaths *J. Phys. D: Appl. Phys.* **50** 23LT02
[26] Lafleur T, Chabert P, Turner M M and Booth J P 2013 Theory for the self-bias formation in capacitively coupled plasmas excited by arbitrary waveforms *Plasma Sources Sci. Technol.* **22** 65013
[27] Donkó Z, Schulze J, Heil B G and Czarnetzki U 2008 PIC simulations of the separate control of ion flux and energy in CCRF discharges via the electrical asymmetry effect *J. Phys. D: Appl. Phys.* **42** 25205
[28] Donkó Z, Schulze J, Czarnetzki U, Derzsi A, Hartmann P, Korolov I and Schüngel E 2012 Fundamental investigations of capacitive radio frequency plasmas: simulations and experiments *Plasma Phys. Control. Fusion* **54** 124003

[29] Brown D L, Walker M L R, Szabo J, Huang W and Foster J E 2017 Recommended practice for use of faraday probes in electric propulsion testing *J. Propuls. Power* **33** 582–613

[30] Su L L and Jorns B A 2021 Performance comparison of a 9-kW magnetically shielded Hall thruster operating on xenon and krypton *J. Appl. Phys.* **130** 163306

[31] Hutchinson I 2002 *Principles of Plasma Diagnostics* (Cambridge: Cambridge University Princeton)

[32] Farnell C C, Farnell C C, Farnell S C and Williams J D 2017 Recommended practice for use of electrostatic analyzers in electric propulsion testing *J. Propuls. Power* **33** 638–58

[33] Huang W and Shastry R 2015 Analysis of Wien filter spectra from Hall thruster plumes *Rev. Sci. Instrum.* **86** 073502

[34] Cedolin R J, Hargus W A Jr, Storm P V, Hanson R K and Cappelli M A 1997 Laser-induced fluorescence study of a xenon Hall thruster *Appl. Phys.* B **65** 459–69

[35] Dale E T 2020 Investigation of the Hall thruster breathing mode (University of Michigan) (available at: (https://hdl.handle.net/2027.42/155282)

[36] Jorns B A, Goebel D M and Hofer R R 2015 Plasma perturbations in high-speed probing of hall thruster discharge chambers: quantification and mitigation *51st AIAA/SAE/ASEE Joint Propulsion Conf. July 2015* (https://doi.org/10.2514/6.2015-4006)

[37] Grimaud L, Pétin A, Vaudolon J and Mazouffre S 2016 Perturbations induced by electrostatic probe in the discharge of Hall thrusters *Rev. Sci. Instrum.* **87** 043506

[38] Romadanov I, Raitses Y, Diallo A, Hara K, Kaganovich I D and Smolyakov A 2018 On limitations of laser-induced fluorescence diagnostics for xenon ion velocity distribution function measurements in Hall thrusters *Phys. Plasmas* **25** 033501

[39] Wegner T, Thompson S J, Williams J and Yalin A P 2021 Two-photon absorption laser induced fluorescence (TALIF) of neutral xenon in a hall effect thruster plasma *AIAA Propulsion and Energy 2021 Forum (August)* p AIAA 2021–3391

[40] de Hoffman E and Stroobant V 2003 *Mass Spectrometry: Principles and Applications* 2nd edn (Toronto: Wiley)

[41] Dirri F, Palomba E, Longobardo A, Zampetti E, Saggin B and Scaccabarozzi D 2019 A review of quartz crystal microbalances for space applications *Sens. Actuators* A **287** 48–75

[42] Yalin A P, Rubin B, Domingue S R, Glueckert Z and Williams J D Differential Sputter Yields Of Boron Nitride, Quartz, and Kapton Due to Low Energy Xe+ Bombardment *AIAA 2007-5314. 43rd AIAA/ASME/SAE/ASEE Joint Propulsion Conference & Exhibit. July 2007* (https://doi.org/10.2514/6.2007-5314)

[43] Sheridan T E 2000 How big is a small Langmuir probe? *Phys. Plasmas* **7** 3084–8

[44] Hershkowitz N 1989 How Langmuir probes work *Plasma Diagnostics* ed O Auciello and D Flamm (New York: Academic)

[45] Takahashi K, Charles C, Boswell R, Lieberman M A and Hatakeyama R 2010 Characterization of the temperature of free electrons diffusing from a magnetically expanding current-free double layer plasma *J. Phys. D: Appl. Phys.* **43** 162001

[46] Godyak V A, Piejak R B and Alexandrovich B M 2002 Electron energy distribution function measurements and plasma parameters in inductively coupled argon plasma *Plasma Sources Sci. Technol.* **11** 525–43

[47] Sudit I D and Chen F F 1994 Rf compensated probes for high-density discharges *Plasma Sources Sci. Technol.* **3** 162–8

[48] Godyak V A, Piejak R B and Alexandrovich B M 1992 Plasma sources science and technology measurement of electron energy distribution in low-pressure RF discharges measurements of electron energy distribution in low-pressure R F discharges *Plasma Sources Sci. Technol.* **18** 36–58

[49] Godyak V 2020 On helicon thrusters: will they ever fly? *J. Appl. Phys.* **127** 103301

[50] Godyak V A and Alexandrovich B M 2015 Comparative analyses of plasma probe diagnostics techniques *J. Appl. Phys.* **118** 233302

[51] Vincent B, Tsikata S, Mazouffre S, Minea T and Fils J 2018 A compact new incoherent thomson scattering diagnostic for low-temperature plasma studies *Plasma Sources Sci. Technol.* **27** 055002

[52] Vincent B, Tsikata S and Mazouffre S 2020 Incoherent thomson scattering measurements of electron properties in a conventional and magnetically-shielded Hall thruster *Plasma Sources Sci. Technol.* **29** 035015

[53] Sheehan J P and Hershkowitz N 2011 Emissive probes *Plasma Sources Sci. Technol.* **20** 063001

[54] Kemp R F and Sellen J M 1966 Plasma potential measurements by electron emissive probes *Rev. Sci. Instrum.* **37** 455–61

[55] Hershkowitz N and Cho M H 1988 Measurement of plasma potential using collecting and emitting probes *J. Vac. Sci. Technol.* A **6** 2054–9

[56] Sheehan J P, Raitses Y, Hershkowitz N and McDonald M 2017 Recommended practice for use of emissive probes in electric propulsion testing *J. Propuls. Power* **33** 614–37

[57] Smith J R, Hershkowitz N and Coakley P 1979 Inflection-point method of interpreting emissive probe characteristics *Rev. Sci. Instrum.* **50** 210–8

[58] Lafleur T, Charles C and Boswell R W 2009 Detailed plasma potential measurements in a radio-frequency expanding plasma obtained from various electrostatic probes *Phys. Plasmas* **16** 044510

[59] Lafleur T 2011 Helicon wave propagation in low diverging magnetic fields (Canberra: Australian National University) (https://doi.org/10.1002/ibd.21393)

[60] Charles C and Boswell R W 2004 Laboratory evidence of a supersonic ion beam generated by a current-free 'helicon' double-layer *Phys. Plasmas* **11** 1706–14

[61] Plihon N, Chabert P and Corr C S 2007 Experimental investigation of double layers in expanding plasmas *Phys. Plasmas* **14** 013506

[62] Harvey Z, Chakraborty Thakur S, Hansen A, Hardin R, Przybysz W S and Scime E E 2008 Comparison of gridded energy analyzer and laser induced fluorescence measurements of a two-component ion distribution *Rev. Sci. Instrum.* **79** 10F314

[63] Lev D *et al* 2019 The technological and commercial expansion of electric propulsion *Acta Astronaut.* **159** 213–27

[64] Fisher J NEXT-C flight ion system status *AIAA Propulsion and Energy 2020 Forum August 2020* (https://doi.org/10.2514/6.2020-3604)

[65] Choueiri E Y 2004 A critical history of electric propulsion: the first fifty years (1906–1956) *J. Propuls. Power* **20** 193–203

[66] Brophy J 2012 The dawn ion propulsion system *The Dawn Mission to Minor Planets 4 Vesta and 1 Ceres* ed C Russell and C Raymond (New York: Springer) pp 251–61

[67] Benkhoff J *et al* 2021 BepiColombo—mission overview and science goals *Space Sci. Rev.* **217** 90

[68] Watanabe S, Tsuda Y, Yoshikawa M, Tanaka S, Saiki T and Nakazawa S 2017 Hayabusa2 mission overview *Space Sci. Rev.* **208** 3–16

[69] O'Reilly D, Herdrich G and Kavanagh D F 2021 Electric propulsion methods for small satellites: a review *Aerospace* **8** 22

[70] Lemmer K 2017 Propulsion for CubeSats *Acta Astronaut.* **134** 231–43

[71] Liang R 2013 The combination of two concentric discharge channels into a nested Hall Effect thruster *PhD Dissertation* University of Michigan (available at: https://hdl.handle.net/2027.42/100043)

[72] Jorns B A and Byrne M P 2021 Model for the dependence of cathode voltage in a Hall thruster on facility pressure *Plasma Sources Sci. Technol.* **30** 015012

[73] Mikellides I G, Katz I, Hofer R R and Goebel D M 2014 Magnetic shielding of a laboratory Hall thruster. I. Theory and validation *J. Appl. Phys.* **115** 0–20

[74] Hofer R R, Goebel D M, Mikellides I G and Katz I 2014 Magnetic shielding of a laboratory Hall thruster. II. Experiments *J. Appl. Phys.* **115** 043304

[75] Hofer R R *et al* 2016 The 12.5 kW Hall effect rocket with magnetic shielding (HERMeS) for the asteroid redirect robotic mission *52nd AIAA/SAE/ASEE Joint Propulsion Conference. July 2016* (https://doi.org/10.2514/6.2016-4825)

[76] Takahashi K *et al* 2011 Direct thrust measurement of a permanent magnet helicon double layer thruster *Appl. Phys. Lett.* **98** 1–4

[77] Takahashi K 2021 Magnetic nozzle radiofrequency plasma thruster approaching twenty percent thruster efficiency *Sci. Rep.* **11** 2768

[78] Sercel J 1993 An experimental and theoretical study of the ECR plasma engine *PhD Thesis* California Institute of Technology

[79] Choueiri E 1998 Scaling of thrust in self-field magnetoplasmadynamic thrusters *J. Propuls. Power* **14** 744–53

[80] Lafleur T 2014 Helicon plasma thruster discharge model *Phys. Plasmas* **21** 043507

[81] Kodys A and Choueiri E A critical review of the state-of-the-art in the performance of applied-field magnetoplasmadynamic thrusters *41st AIAA/ASME/SAE/ASEE Joint Propulsion Conf. and Exhibit (July 2005)* p AIAA 2005–4247

[82] National Academies of Science 2021 *Space Nuclear Propulsion for Human Mars Exploration* (Washington, DC: The National Academies Press) (https://doi.org/10.17226/25977)

[83] Toki K, Shimuzu Y and Kuriki K 1997 Electric propulsion experiment (EPEX) of a repetitively pulsed MPD thruster system onboard space flyer unit (SFU) *25th Int. Electric Propulsion Conf.* pp 749–55

[84] Voronov A S, Troitskiy A A, Egorov I D, Samoilenkov S V and Vavilov A P 2020 Magnetoplasmadynamic thruster with an applied field based on the second generation high-temperature superconductors *J. Phys.: Conf. Ser.* **1686** 12023

[85] Boxberger A, Behnke A and Herdrich G 2019 Current advances in optimization of operative regimes of steady state applied field MPD thrusters *Proc. 36th Int. Electric Propulsion Conf. IEPC-2019-585*

[86] Zheng J *et al* 2021 Integrated study on the comprehensive magnetic-field configuration performance in the 150 kW superconducting magnetoplasmadynamic thruster *Sci. Rep.* **11** 20706

[87] Lee C G N, Kanarik K J and Gottscho R A 2014 The grand challenges of plasma etching: a manufacturing perspective *J. Phys. D: Appl. Phys.* **47** 273001

[88] Coburn J W and Winters H F 1979 Ion- and electron-assisted gas-surface chemistry—an important effect in plasma etching *J. Appl. Phys.* **50** 3189–96

[89] Winters H F and Coburn J W 1992 Surface science aspects of etching reactions *Surf. Sci. Rep.* **14** 162–269

[90] Donnelly V M and Kornblit A 2013 Plasma etching: yesterday, today, and tomorrow *J. Vac. Sci. Technol.* A **31** 050825

[91] Oehrlein G S and Kurogi Y 1998 Sidewall surface chemistry in directional etching processes *Mater. Sci. Eng.* R **24** 153–83

[92] Bouchoule S, Patriarche G, Guilet S, Gatilova L, Largeau L and Chabert P 2008 Sidewall passivation assisted by a silicon coverplate during Cl2–H2 and HBr inductively coupled plasma etching of InP for photonic devices *J. Vac. Sci. Technol.* B **26** 666–74

[93] Aachboun S and Ranson P 1999 Deep anisotropic etching of silicon *J. Vac. Sci. Technol.* A **17** 2270–3

[94] Marty F, Rousseau L, Saadany B, Mercier B, Français O, Mita Y and Bourouina T 2005 Advanced etching of silicon based on deep reactive ion etching for silicon high aspect ratio microstructures and three-dimensional micro- and nanostructures *Microelectron. J.* **36** 673–7

[95] Kessels E *et al* 2022 *Plasma Sources Sci. Technol.* **31** 103002

[96] Martinu L and Poitras D 2000 Plasma deposition of optical films and coatings: a review *J. Vac. Sci. Technol.* A **18** 2619–45

[97] Huang H, Winchester K J, Suvorova A, Lawn B R, Liu Y, Hu X Z, Dell J M and Faraone L 2006 Effect of deposition conditions on mechanical properties of low-temperature PECVD silicon nitride films *Mater. Sci. Eng.* A **435–436** 453–9

[98] Schmitt J, Elyaakoubi M and Sansonnens L 2002 Glow discharge processing in the liquid crystal display industry *Plasma Sources Sci. Technol.* **11** A206–10

[99] Bucio T D, Khokhar A Z, Lacava C, Stankovic S, Mashanovich G Z, Petropoulos P and Gardes F Y 2016 Material and optical properties of low-temperature NH_3-free PECVD SiN_x layers for photonic applications *J. Phys. D: Appl. Phys.* **50** 25106

[100] Soppe W, Rieffe H and Weeber A 2005 Bulk and surface passivation of silicon solar cells accomplished by silicon nitride deposited on industrial scale by microwave PECVD *Prog. Photovolt. Res. Appl.* **13** 551–69

[101] Meyyappan M, Delzeit L, Cassell A and Hash D 2003 Carbon nanotube growth by {PECVD}: a review *Plasma Sources Sci. Technol.* **12** 205–16

[102] Gudmundsson J T *et al* 2022 *Plasma Sources Sci. Technol.* **31** 083001

[103] Snyders R 2022 Foundations of plasma synthesis using plasma enhanced chemical vapor deposition *Plasma Sources Sci. Technol.*

[104] Bundesmann C and Neumann H 2018 Tutorial: the systematics of ion beam sputtering for deposition of thin films with tailored properties *J. Appl. Phys.* **124** 231102

[105] Harper J M E, Cuomo J J and Kaufman H R 1982 Technology and applications of broad-beam ion sources used in sputtering. Part II. Applications *J. Vac. Sci. Technol.* **21** 737–56

[106] Martin P M (ed) 2010 *Handbook of Deposition Technologies for Films and Coatings* 3rd edn (Boston: William Andrew Publishing)

[107] Erler H-J, Reisse G and Weissmantel C 1980 Nitride film deposition by reactive ion beam sputtering *Thin Solid Films* **65** 233–45

[108] Williams J S 1998 Ion implantation of semiconductors *Mater. Sci. Eng.* A **253** 8–15

[109] Larson L A, Williams J M and Current M I 2012 Ion implantation for semiconductor doping and materials

modification *Rev. Accel. Sci. Technol. Accel. Appl. Ind. Environ.* **4** 11–40
[110] Anders A 2020 *Handbook of Plasma Immersion Ion Implantation and Deposition* (New York: Wiley)
[111] Chu P K 2004 Recent developments and applications of plasma immersion ion implantation *J. Vac. Sci. Technol.* B **22** 289–96
[112] Huang N, Yang P, Leng Y X, Wang J, Sun H, Chen J Y and Wan G J 2004 Surface modification of biomaterials by plasma immersion ion implantation *Surf. Coat. Technol.* **186** 218–26
[113] Tian X B, Wei C B, Yang S Q, Fu R K Y and Chu P K 2005 Corrosion resistance improvement of magnesium alloy using nitrogen plasma ion implantation *Surf. Coat. Technol.* **198** 454–8
[114] Kaufman H R, Cuomo J J and Harper J M E 1982 Technology and applications of broad-beam ion sources used in sputtering. Part I. Ion source technology *J. Vac. Sci. Technol.* **21** 725–36
[115] Melngailis J 1987 Focused ion beam technology and applications *J. Vac. Sci. Technol.* B **5** 469–95
[116] Winiarski B, Gholinia A, Mingard K, Gee M, Thompson G E and Withers P J 2017 Broad ion beam serial section tomography *Ultramicroscopy* **172** 52–64
[117] Hanke L D, Schenk K H and Scholz D 2016 Broad beam ion milling for microstructure characterization *Mater. Perform. Charact.* **5** 20160049
[118] Aalto T *et al* 2010 List of contributors *Handbook of Silicon Based MEMS Materials and Technologies* ed V Lindroos *et al* (Boston: William Andrew Publishing) pp xi–xiii
[119] Schulze C, Nestler M and Zeuner M 2019 Ion-beam figuring of x-ray mirrors *Astron Optical: Design Manufacturing Test Space Ground System II* vol 11116 pp 314–24
[120] Godyak V A, Piejak R B and Alexandrovich B M 1991 Electrical characteristics of parallel-plate RF discharges in argon *IEEE Trans. Plasma Sci.* **19** 660–76
[121] Perret A, Chabert P, Jolly J and Booth J P 2005 Ion energy uniformity in high-frequency capacitive discharges *Appl. Phys. Lett.* **86** 021501
[122] Keller J H 1996 Inductive plasmas for plasma processing *Plasma Sources Sci. Technol.* **5** 166–72
[123] Piejak R B, Godyak V A and Alexandrovich B M 1992 A simple analysis of an inductive RF discharge *Plasma Sources Sci. Technol.* **1** 179–86
[124] Lieberman M A and Gottscho R A 1994 Design of high-density plasma sources for materials processing *Phys. Thin films* **1994** 1–119
[125] Rafalskyi D *et al* 2021 In-orbit demonstration of an iodine electric propulsion system *Nature* **599** 411–5
[126] Holste K *et al* 2020 Ion thrusters for electric propulsion: scientific issues developing a niche technology into a game changer *Rev. Sci. Instrum.* **91** 061101
[127] Kaufman H R and Harper J M 2004 Ion-assist applications of broad-beam ion sources *SPIE Proceeding* 5527
[128] Zeuner M, Scholze F, Neumann H, Chassé T, Otto G, Roth D, Hellmich A and Ocker B 2001 A unique ECR broad beam source for thin film processing *Surf. Coat. Technol.* **142–144** 11–20
[129] Zeuner M, Scholze F, Dathe B and Neumann H 2001 Optimisation and characterisation of a TCP type RF broad beam ion source *Surf. Coat. Technol.* **142–144** 39–48
[130] Gudmundsson J T 2020 Physics and technology of magnetron sputtering discharges *Plasma Sources Sci. Technol.* **29** 113001
[131] Gudmundsson J T, Brenning N, Lundin D and Helmersson U 2012 High power impulse magnetron sputtering discharge *J. Vac. Sci. Technol.* A **30** 030801
[132] Alami J, Gudmundsson J T, Bohlmark J, Birch J and Helmersson U 2005 Plasma dynamics in a highly ionized pulsed magnetron discharge *Plasma Sources Sci. Technol.* **14** 525–31
[133] Lundin D and Sarakinos K 2012 An introduction to thin film processing using high-power impulse magnetron sputtering *J. Mater. Res.* **27** 780–92
[134] Dale E, Jorns B and Gallimore A 2020 Future directions for electric propulsion research *Aerospace* **7** 1–30
[135] Hall S J *et al* 2022 Performance and High-Speed Characterization of a 100-kW Nested Hall Thruster *J. Propuls. Power* 40–50
[136] Patterson M J, Herman D, Shastry R, Van Noord J and Foster J E 2012 Annular-geometry ion engine: concept, development status, and preliminary performance *48th AIAA/ASME/SAE/ASEE Joint Propulsion Conf. Exhibit July 2012* (https://doi.org/10.2514/6.2012-3798)
[137] Squire J P *et al* 2013 VASIMR® spaceflight engine system mass study and scaling with power *33rd Int. Electric Propulsion Conf.* (*May 2014*) pp IEPC-2013-149
[138] Zheng P, Wu J, Zhang Y and Wu B 2020 A comprehensive review of atmosphere-breathing electric propulsion systems *Int. J. Aerosp. Eng.* **2020** 21
[139] Rovey J L, Lyne C T, Mundahl A J, Rasmont N, Glascock M S, Wainwright M J and Berg S P 2020 Review of multimode space propulsion *Prog. Aerosp. Sci.* **118** 100627
[140] Randolph T, Kim V, Kaufman H, Kozubsky K, Zhurin V and Day M 1993 Facility effects on stationary plasma thruster testing *Proc. 23rd Int. Electric Propulsion Conf.* IEPC-93-93
[141] Byers D and Dankanich J 2009 A review of facility effects on Hall effect thrusters *31st Int. Electric Propulsion Conf.* IEPC-2009-076
[142] Hofer R R and Anderson J R 2014 Finite pressure effects in magnetically shielded hall thrusters *50th AIAA/ASME/SAE/ASEE Joint Propulsion Conf. July 2014* AIAA-2014-3709 (https://doi.org/10.2514/6.2014-3709)
[143] Frieman J D, Walker J A, Walker M L R, Khayms V and King D Q 2016 Electrical facility effects on Hall thruster cathode coupling: performance and plume properties *J. Propuls. Power* **32** 251–64
[144] Brophy J, Polk J, Randolph T and Dankanich J 2008 Lifetime qualification standards for electric thrusters for deep-space missions *44th AIAA Joint Propulsion Conf. and Exhibit July 2008* AIAA-2008-5184 (https://doi.org/10.2514/6.2008-5184)
[145] Plasma science 2020 decadal survey: overview and opportunities for the low temperature plasma community
[146] Boeuf J-P 2017 Tutorial: physics and modeling of Hall thrusters *J. Appl. Phys.* **121** 011101
[147] Semiconductor Industry Association 2015 *International Technology Roadmap for Semiconductors 2.0* (available at: www.semiconductors.org/main/2015_international_technology_roadmap_for_semiconductors_itrs/)
[148] Kim H 2011 Characteristics and applications of plasma enhanced-atomic layer deposition *Thin Solid Films* **519** 6639–44
[149] Rossnagel S M, Sherman A and Turner F 2000 Plasma-enhanced atomic layer deposition of Ta and Ti for interconnect diffusion barriers *J. Vac. Sci. Technol.* B **18** 2016
[150] Faraz T, Arts K, Karwal S, Knoops H C M and Kessels W M M 2019 Energetic ions during plasma-enhanced atomic layer deposition and their role in tailoring material properties *Plasma Sources Sci. Technol.* **28** 024002
[151] Kanarik K J, Lill T, Hudson E A, Sriraman S, Tan S, Marks J, Vahedi V and Gottscho R A 2015 Overview of atomic

layer etching in the semiconductor industry *J. Vac. Sci. Technol.* A **33** 020802
[152] Oehrlein G S, Metzler D and Li C 2015 Atomic layer etching at the tipping point: an overview *ECS J. Solid State Sci. Technol.* **4** N5041–53
[153] Ohba T, Yang W, Tan S, Kanarik K J and Nojiri K 2017 Atomic layer etching of GaN and AlGaN using directional plasma-enhanced approach *Jpn. J. Appl. Phys.* **56** 06HB06
[154] Samukawa S 2006 Ultimate top-down etching processes for future nanoscale devices: advanced neutral-beam etching *Jpn. J. Appl. Phys.* **45** 2395–407
[155] Walton S G, Boris D R, Hernández S C, Lock E H, Petrova T B, Petrov G M and Fernsler R F 2015 Electron beam generated plasmas for ultra low T_e processing *ECS J. Solid State Sci. Technol.* **4** N5033–40
[156] Lieberman M A, Booth J P, Chabert P, Rax J M and Turner M M 2002 Standing wave and skin effects in large-area, high-frequency capacitive discharges *Plasma Sources Sci. Technol.* **11** 310
[157] Goto H, Sasaki M, Ohmi T, Shibata T, Yamagami A, Okamura N and Kamiya O 1990 Minimizing wafer surface damage and chamber material contamination in new plasma processing equipment *Jpn. J. Appl. Phys.* **29** L2395–7
[158] Donkó Z, Schulze J, Hartmann P, Korolov I, Czarnetzki U and Schüngel E 2010 The effect of secondary electrons on the separate control of ion energy and flux in dual-frequency capacitively coupled radio frequency discharges *Appl. Phys. Lett.* **97** 081501
[159] Gans T, Schulze J, O'Connell D, Czarnetzki U, Faulkner R, Ellingboe A R and Turner M M 2006 Frequency coupling in dual frequency capacitively coupled radio-frequency plasmas *Appl. Phys. Lett.* **89** 261502
[160] Lafleur T 2016 Tailored-waveform excitation of capacitively coupled plasmas and the electrical asymmetry effect *Plasma Sources Sci. Technol.* **25** 013001
[161] Bruneau B, Gans T, O'Connell D, Greb A, Johnson E V and Booth J-P 2015 Strong ionization asymmetry in a geometrically symmetric radio frequency capacitively coupled plasma induced by sawtooth voltage waveforms *Phys. Rev. Lett.* **114** 125002
[162] Lafleur T, Delattre P A, Johnson E V and Booth J P 2012 Separate control of the ion flux and ion energy in capacitively coupled radio-frequency discharges using voltage waveform tailoring *Appl. Phys. Lett.* **101** 124104
[163] Bruneau B, Lafleur T, Booth J-P and Johnson E 2016 Controlling the shape of the ion energy distribution at constant ion flux and constant mean ion energy with tailored voltage waveforms *Plasma Sources Sci. Technol.* **25** 025006
[164] Schüngel E, Mohr S, Schulze J and Czarnetzki U 2015 Prevention of ion flux lateral inhomogeneities in large area capacitive radio frequency plasmas via the electrical asymmetry effect *Appl. Phys. Lett.* **106** 054108
[165] Schmidt F *et al* 2018 Multi frequency matching for voltage waveform tailoring *Plasma Sources Sci. Technol.* **27** 095012
[166] Wang J, Dine S, Booth J-P and Johnson E V 2019 Experimental demonstration of multifrequency impedance matching for tailored voltage waveform plasmas *J. Vac. Sci. Technol.* A **37** 021303
[167] Schüngel E, Hofmann R, Mohr S, Schulze J, Röpcke J and Czarnetzki U 2015 Evaluation of the electrical asymmetry effect by spectroscopic measurements of capacitively coupled discharges and silicon thin film depositions *Thin Solid Films* **574** 60–65